

Design of a Piecewise-Stiffening Nonlinear Energy Sink for Torsional Vibration Attenuation

Harikrishnan Venugopal^{a,*}, Mia Loccufier^a, Kevin Dekemele^a

^aGhent University, Department of Electromechanical, Systems and Metal Engineering, Tech Lane Ghent Science Park - Campus A-46, Ghent, 9052, Belgium

Abstract

Torsional vibrations are undesirable in rotating machinery, and demands for better performance and material savings to reduce weight exacerbate this issue by triggering resonance conditions. The Nonlinear Energy Sink (NES) offers a robust and effective vibration attenuation solution. In this research, a 2 Degree-Of-Freedom torsionally vibrating host structure is equipped with a NES having piecewise-linear stiffness approximating a cubic nonlinearity. The first-order Complexification-Averaging (CxA) method is used to analyse the Slow Flow dynamics on the response envelope, and a NES tuning methodology based on the Slow Invariant Manifold is proposed for 1:1 resonance attenuation for two resonance frequencies of the host system. The mechanical design of the NES is optimised for minimal stresses and fatigue while avoiding local resonances of the individual components. Experiments and numerical simulations validate the CxA method, and indicate the presence of Strongly Modulated Response regime and an Isolated Resonance Curve in the vicinity of resonance. Significant resonant response attenuation is achieved for both the first mode ($> 80\%$) and the second mode ($> 65\%$) over a wide range of forcing amplitudes, with possibility of further improvements. In this regard, design modifications that allow for effective multi-modal attenuation are presented. As such, a complete toolchain has been developed to obtain an NES design which can be applied to a wide range of torsional vibration applications.

Keywords: Torsional vibration, Design optimisation, Modal reduction, Nonlinear Energy Sink, Piecewise linearity, Complexification-Averaging

1. Introduction

Torsional vibration attenuation plays a crucial role in the design of power transmissions, turbomachinery, and other rotating machinery. As industry trends towards sustainability push for lightweight machinery, to meet the need for improved fuel efficiency and performance, the operational range of the system comes closer to its undesirable resonances, increasing vibration amplitudes. This is particularly important for rotating machinery since shear stress caused by torsion has a lower fatigue limit for failure than bending/tensile stress. A selection of research in torsional vibration analysis and material fatigue is presented in [1, 2, 3, 4, 5]. Suitable care must be taken during the design stage to mitigate these issues.

A potential approach is to use vibration absorbers tuned to absorb the resonant vibrations of the primary/host system. Frahm [6] proposed the first version of the Tuned Mass Damper (TMD) as a passive auxiliary attachment on

*Corresponding author

Email address: harikrishnan.venugopal@ugent.be (Harikrishnan Venugopal)

the host. This concept was later improved by Den Hartog [7], who also proposed an optimal damping criterion. Later developments in the field of vibration mitigation have seen the emergence of electromechanical actuation, resulting in the creation of active [8, 9, 10, 11] and semi-active [12, 13, 14, 15, 16] vibration absorbers. Although a well-designed active control strategy promises significant vibration attenuation, the requirement for an external power source is a drawback and stability may not be guaranteed. A number of TMD variations have been investigated previously in relation to torsional vibrations, including the Dual-Mass Flywheel [17], the speed-dependent absorbers [18, 19] and the Damped Pulley Absorber [20]. A TMD's main disadvantages are its limited frequency band of attenuation and the presence of side resonances. Over the last two decades, it has been found that incorporating nonlinear components into the vibration absorber can significantly enhance its robustness and operating range compared to conventional TMDs.

The nonlinear vibration absorber, also known as a Nonlinear Energy Sink (NES), has several advantages compared to its linear equivalents: (1) it can work effectively even when the host system has undergone perturbations to its parameters, and (2) the nonlinearity allows the device to attenuate multiple resonant frequencies of the host system [21, 22, 23, 24]. The former property of 'de-tuning' supports its robustness and the latter supports its role as a broadband absorber. Unlike the Tuned Mass Damper (TMD), the NES does not generate side resonances or an antiresonant response. Instead, it produces a resonant response with amplitude saturation. The NES has a variable natural frequency that depends on the level of excitation, allowing it to self-tune to the host system's frequency. In the case of transient excitations, the NES initiates Targeted Energy Transfer (TET), which involves an irreversible transfer of energy to the NES, with the energy being subsequently dissipated through damping [25, 26, 24, 27]. Under harmonic excitations at 1:1 resonance, a quasi-periodic response resembling relaxation oscillations occur [22, 21, 28], referred to as the Strongly Modulated Response (SMR). Another potentially hazardous bifurcation from a harmonic excitation is the attraction to an Isolated Resonance Curve (IRC) [29, 30], which can lead to a sudden increase in vibrations and could be triggered by an additional impulse or shock excitation. Accurate characterisation of such bifurcating responses is essential for the robust implementation of the NES. Despite these requirements, NES technology has become increasingly popular in recent years since its introduction by Vakakis [31] in 2001.

Examples of NES implementations are extensive. Significant progress has been made in the area of seismic vibration mitigation [32, 33, 34, 35], where robustness to changes in the host structure, multi-modal broadband attenuation, and multi-directional vibration reduction are desired. In the aerospace sector [36, 37, 38] there is also a focus on flutter-induced instability mitigation. In the manufacturing domain [39, 40], the control of chatter-induced instability is a key concern. The NES has also been used to mitigate vibrations in continuous systems, such as bridge cables [41], beams [42, 43] and plates subjected to aerodynamic forces [44, 45, 46]. A comprehensive review of NES technology is presented in [47, 48].

Several non-linear stiffness and damping variations of the NES have been studied for their potential. In this aspect, the cubic [49, 23, 50], the softening [51, 52, 53], the saturating [51, 54], the periodic [55, 56], the bistable [57, 58, 59, 60, 35, 61], and the tristable [62, 63, 64] stiffness characteristics are of particular interest. The recent development of a quasi-zero stiffness characteristics for multi-directional vibration attenuation is also noteworthy [65, 66]. Here, the NES design facilitates the mitigation of low-frequency vibrations and accommodates large excitation amplitudes. Similarly, variations in nonlinear viscous damping are also explored [67, 68, 58]. The type of nonlinearity chosen affects the order of attenuation of resonances and the energy threshold required to initiate TET/SMR. Regarding solution methods, analytical techniques such as Harmonic Balancing (HB) [69] and Complexification-Averaging (CxA) [70, 24, 71] have gained considerable popularity in the analysis of nonlinear systems, as they provide more insightful

results compared to numerical methods.

Recent studies have highlighted the effectiveness of NES in reducing torsional vibrations. A previous study by Haris et al. [72] examined the performance of cubic, quintic, and vibro-impact NES for their effectiveness in attenuating torsional vibrations, with experimental and numerical validation [73]. Cao et al. introduced a piecewise-linear stiffness NES connected to an inerter mechanism, which demonstrated considerable suppression of resonant vibrations while maintaining a low NES mass [74]. The same researchers have employed similar methodologies to induce nonlinearity in the NES for attenuating both transient and harmonic excitations [75, 76], as well as for the design of a multi-stable NES [77]. Furthermore, innovative designs that incorporate nonlinearity through permanent magnets [78, 79] and via particle dampers[80] have been studied; significant reductions in vibration amplitude and suppression time are reported here. A recent work by Cao et al. also showcased a piecewise-linear stiffness NES capable of multi-modal torsional vibration attenuation [81], with a tuning methodology based on a numerically evaluated energy dissipation measure. The same author presents a piecewise-stiffening NES to mitigate multi-modal transient vibrations of a torsional system though Resonance Capture Cascade [82]. Ma et al. present a comparison of monostable, bistable, and tristable stiffness configurations, all realised within an adaptable single NES mechanism, aimed at mitigating torsional vibration [83]. The examples of NES implementations mentioned above demonstrate its potential to mitigate torsional vibrations.

The latest advancements in NES technology demonstrate innovative concepts, yet they often lack a link to practical implementation through optimal design configurations that consider strength, fatigue, and local resonances of the design. In this paper, these design aspects are integrated with analytical techniques, design optimisation and experiments. Another aspect is the novelty of using entirely analytical techniques to fully explore the behaviour of the experimental dynamical system and to validate the design's performance. This approach is computationally less demanding than numerical methods and can uncover behaviour that numerical simulations and experiments may overlook. Additionally, several tests for investigating the influence of assumptions within the analytical method are included. In this paper, the NES design is based on a cubic stiffness approximated by the piecewise engagement of linear members, proposed by Cao et al.[76], but with a focus on analytical computation of the systems' response for tuning the NES parameters, and addressing the practical considerations of strength and durability of the design. As such, a complete toolchain is presented that, from analytical model to realisation, can be easily adapted by designers of other torsional systems.

The organisation of the paper is as explained here. Section 2 explains the dynamic model of the host system with the NES attached to an arbitrary location. The equations of motion are projected on the mode to be attenuated. The analytical solutions are derived using the CxA method, extracting the slow dynamics of the oscillation envelope from the reduced NES-host system. The Frequency Response (FR) and Slow Invariant Manifold (SIM)(s) are obtained, and bifurcation analysis and parameter influence are presented. The tuning of the NES based on the SIM is also presented. Section 3 describes the concept of the piecewise-stiffening NES and contains computations for the local stress and resonance conditions. Thereafter, a design optimisation problem is discussed for minimising local stresses and avoiding local resonances while adhering to the NES stiffness from the tuning. Next, Section 4 starts with the procedure for identifying the parameters of experimental NES-host system. A numerical validation of the CxA method is presented, comparing the NES with cubic stiffness and piecewise-stiffening nonlinearity. The vibration mitigation performance of the NES is investigated experimentally for the first mode of the host system, with results closely matching the CxA predictions. Similarly, Section 5 examines the mitigation performance for the second mode of the host system, and design adaptations for the NES are discussed to improve performance. Finally, section 6 presents a

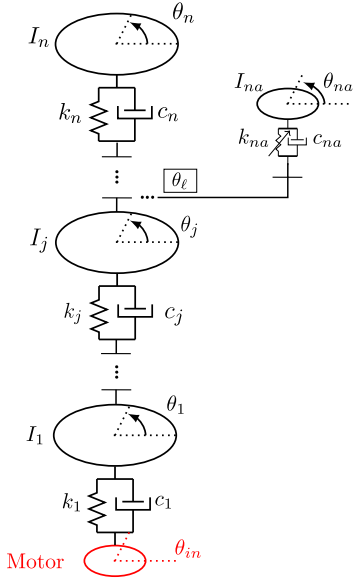


Figure 1: The scheme of the dynamical model of an n -Degree-Of-Freedom (DOF) torsional host system attached with a Nonlinear Energy Sink (NES). Each inertia of the host has a corresponding shaft stiffness and damping coefficient. The host is excited by a motor at the first DOF (inertia I_1). The intermediary DOFs are indexed as j ($1 < j < n$). The NES is attached to an arbitrary host DOF (ℓ) and is defined through an inertia I_{na} , a cubic stiffness coefficient k_{na} , and linear damping coefficient c_{na} .

discussion and conclusion that highlights the advantages of a tuned NES, as well as the bifurcating responses that can be detrimental to its overall performance.

2. Dynamic model description

The vibration response of a structure with a NES is described through the study of its dynamic model. Consider a linear n -Degrees-Of-Freedom (n -DOF) host system with the NES attached to an arbitrary host DOF. Modal reduction is performed on the Equations of Motion (EOM) of the host system, with focus on the vibration mode targeted for mitigation by the NES. This implies that the NES will be tuned to attenuate the i^{th} mode of the host in 1:1 resonance capture. The resulting EOM is made dimensionless such that the results retain generality. In addition, the envelope of oscillation is studied using the CxA method, where the invariant manifolds of the Slow Flow dynamics are obtained. The fixed points of the Slow Flow, and their stability, are then used to explain the behaviour of the NES-host system. A parameter analysis of the Slow Flow dynamics is presented, following which NES tuning is discussed for mitigating the first mode of the host.

2.1. Equations of motion

A n -DOF torsional host system is shown in Fig. 1, where a cubic stiffness NES is attached to an arbitrary DOF ℓ . The host DOFs are defined by angle θ_i for the i^{th} arbitrary DOF with an associated torsional stiffness k_i and linear damping c_i . The NES is defined by angular displacement θ_{na} , linear damping c_{na} and cubic stiffness coefficient k_{na} .

The resulting EOM is of the following form:

$$\begin{aligned} I_1 \ddot{\theta}_1 + k_1 \theta_1 + c_1 \dot{\theta}_1 + c_2 (\dot{\theta}_1 - \dot{\theta}_2) + k_2 (\theta_1 - \theta_2) + \delta_{\ell,1} (I_{\text{na}} \ddot{\theta}_{\text{na}}) &= F_1 \cos(\omega t) \\ I_j \ddot{\theta}_j + k_j (\theta_j - \theta_{j-1}) + c_j (\dot{\theta}_j - \dot{\theta}_{j-1}) + c_{j+1} (\dot{\theta}_j - \dot{\theta}_{j+1}) + k_{j+1} (\theta_j - \theta_{j+1}) + \delta_{\ell,j} (I_{\text{na}} \ddot{\theta}_{\text{na}}) &= F_j \cos(\omega t), \quad 1 < j < n \\ I_n \ddot{\theta}_n + k_n (\theta_n - \theta_{n-1}) + c_n (\dot{\theta}_n - \dot{\theta}_{n-1}) + \delta_{\ell,n} (I_{\text{na}} \ddot{\theta}_{\text{na}}) &= F_n \cos(\omega t) \\ I_{\text{na}} \ddot{\theta}_{\text{na}} + k_{\text{na}} (\theta_{\text{na}} - \theta_{\ell})^3 + c_{\text{na}} (\dot{\theta}_{\text{na}} - \dot{\theta}_{\ell}) &= 0 \end{aligned} \quad (1)$$

where,

$$\delta_{\ell,m} = \begin{cases} 1 & \text{for } m = \ell \\ 0 & \text{for } m \neq \ell \end{cases}$$

Here, j ($1 < j < n$) denotes an intermediary DOF of the host and, $\delta_{\ell,m}$ is a NES connection variable that equals 1 for the desired attachment DOF ($m = \ell$). The force F_1 applied to the inertia I_1 is related to the imposed sinusoidal motor angle θ_{in} as follows:

$$F_1 \cos(\omega t) = k_1 \theta_{in} + c_1 \dot{\theta}_{in} \approx k_1 \theta_{in} \quad (2)$$

The above equations can be condensed into the following matrix form:

$$\begin{aligned} \mathbf{I} \ddot{\theta} + \mathbf{C} \dot{\theta} + \mathbf{K} \theta + \delta_{\ell} (I_{\text{na}} \ddot{\theta}_{\text{na}}) &= \mathbf{F} \cos(\omega t) \\ I_{\text{na}} \ddot{\theta}_{\text{na}} + c_{\text{na}} (\theta_{\text{na}} - \theta_{\ell}) + k_{\text{na}} (\theta_{\text{na}} - \theta_{\ell})^3 &= 0 \end{aligned} \quad (3)$$

The rotational inertia matrix $\mathbf{I} \in \mathbb{R}^{n \times n}$, torsional stiffness matrix $\mathbf{K} \in \mathbb{R}^{n \times n}$ and the angular displacement vector $\theta \in \mathbb{R}^{n \times 1}$ are given in Eq. (4) below. Note that the host system is assumed to be proportionally damped, therefore $\mathbf{C} = \alpha_c \mathbf{I} + \beta_c \mathbf{K}$, where α_c and β_c are constants of proportionality. $\mathbf{F} \in \mathbb{R}^{n \times 1}$ is the force vector.

$$\mathbf{I} = \begin{bmatrix} I_1 & \cdots & 0 \\ \vdots & \ddots & \vdots \\ 0 & \cdots & I_n \end{bmatrix}_{n \times n} \quad \mathbf{K} = \begin{bmatrix} k_1 + k_2 & -k_2 & \cdots & & 0 \\ -k_2 & k_2 + k_3 & -k_3 & \cdots & 0 \\ \vdots & \ddots & \ddots & \ddots & \vdots \\ 0 & -k_j & k_j + k_{j+1} & -k_{j+1} & 0 \\ \vdots & & \ddots & \ddots & \vdots \\ 0 & \cdots & \cdots & \cdots & -k_n & k_n \end{bmatrix}_{n \times n} \quad \theta = \begin{bmatrix} \theta_1 \\ \vdots \\ \theta_j \\ \vdots \\ \theta_n \end{bmatrix}_{n \times 1} \quad (4)$$

The following eigenvalue problem is obtained from the undamped, unforced host system without the NES attached:

$$\det(\mathbf{K} - \mathbf{I}\omega_i^2) = 0 \quad (\mathbf{K} - \mathbf{I}\omega_i^2)\mathbf{e}_i = 0 \quad (5)$$

where ω_i^2 is the eigenvalue and $\mathbf{e}_i \in \mathbb{R}^{n \times 1}$ is the eigenvector corresponding to an arbitrary mode i of the host (the index i will refer to the i^{th} modal parameters henceforth). It is worth mentioning that proportional damping allows modal decoupling of the host EOM using the same modes found from the undamped eigenvalue problem. Performing modal transformation $\theta = \mathbf{E}q$ in the first equation of Eq. (3), with $\mathbf{E} = [\mathbf{e}_1, \mathbf{e}_2, \dots, \mathbf{e}_n]$ and pre-multiplying with \mathbf{E}^T , the host

EOM is decoupled as shown in Eq. (6). The NES connection vector is modified as $e_i(\ell) = \mathbf{e}_i^T \delta_\ell$.

$$\begin{aligned} I_{q,i}\ddot{q}_i + c_{q,i}\dot{q}_i + k_{q,i}q_i + e_i(\ell)(I_{\text{na}}\dot{\theta}_{\text{na}}) &= \mathbf{e}_i^T \mathbf{F} \cos(\omega t) \quad \text{for } i = [1, \dots, n] \\ I_{\text{na}}\ddot{\theta}_{\text{na}} + c_{\text{na}}(\dot{\theta}_{\text{na}} - \dot{\theta}_\ell) + k_{\text{na}}(\theta_{\text{na}} - \theta_\ell)^3 &= 0 \end{aligned} \quad (6)$$

The host dynamics is reduced around a single mode i , whose resonance condition is to be mitigated by the NES in 1:1 resonance capture. The effect of the NES on other modes is not considered. Equation (6) is rewritten as shown below, with the NES attachment coordinate being modified as $\theta_\ell = q_i e_i(\ell)$.

$$\begin{aligned} \frac{I_{q,i}}{e_i(\ell)^2}\ddot{\theta}_\ell + \frac{c_{q,i}}{e_i(\ell)^2}\dot{\theta}_\ell + \frac{k_{q,i}}{e_i(\ell)^2}\theta_\ell + (I_{\text{na}}\dot{\theta}_{\text{na}}) &= \frac{F_m}{e_i(\ell)} \cos(\omega t) \\ I_{\text{na}}\ddot{\theta}_{\text{na}} + c_{\text{na}}(\dot{\theta}_{\text{na}} - \dot{\theta}_\ell) + k_{\text{na}}(\theta_{\text{na}} - \theta_\ell)^3 &= 0 \end{aligned} \quad (7)$$

Where $F_m = \mathbf{e}_i^T \mathbf{F}$ is the magnitude of the i^{th} modal force. Defining the host angle at the ℓ^{th} DOF as $\theta_\ell = y$, the relative absorber angle as $z = \theta_{\text{na}} - y$, and dividing Eq. (7) by $\frac{I_{q,i}}{e_i(\ell)^2}$ we get:

$$\begin{aligned} \ddot{y} + \varepsilon\xi\omega_i\dot{y} + \omega_i^2y + \varepsilon(\ddot{z} + \ddot{y}) &= \varepsilon\omega_i^2P \cos(\omega t) \\ \varepsilon(\ddot{z} + \ddot{y}) + \varepsilon\xi_{\text{na}}\omega_i\dot{z} + \varepsilon\omega_i^2\gamma z^3 &= 0 \end{aligned} \quad (8)$$

where,

$$\begin{aligned} \varepsilon &= \frac{I_{\text{na}}e_i^2(\ell)}{I_{q,i}} [-] \quad \omega_i^2 = \frac{k_{q,i}}{I_{q,i}} \left[\frac{1}{s^2} \right] \quad \xi = \frac{c_{q,i}}{I_{\text{na}}\omega_i} [-] \\ \xi_{\text{na}} &= \frac{c_{\text{na}}}{I_{\text{na}}\omega_i e_i^2(\ell)} [-] \quad \gamma = \frac{k_{\text{na}}}{I_{\text{na}}\omega_i^2} [-] \quad P = \frac{F_m}{I_{\text{na}}\omega_i^2 e_i(\ell)} [-] \end{aligned} \quad (9)$$

Finally, the time and motion are made dimensionless by the following substitution:

$$\tau = \omega_i t \quad \bar{y} = \sqrt{\gamma}y \quad \bar{z} = \sqrt{\gamma}z$$

Following which Eq. (8) becomes,

$$\begin{aligned} \ddot{\bar{y}}' + \varepsilon\xi\bar{y}' + \bar{y} + \varepsilon(\ddot{\bar{z}}' + \ddot{\bar{y}}') &= \varepsilon\bar{P} \cos(\Omega\tau) \\ \varepsilon(\ddot{\bar{z}}' + \ddot{\bar{y}}') + \varepsilon\xi_{\text{na}}\bar{z}' + \varepsilon\bar{z}^3 &= 0 \end{aligned} \quad (10)$$

where

$$()' = \frac{\partial()}{\partial\tau} \quad \Omega = \frac{\omega}{\omega_i} \quad \bar{P} = \sqrt{\gamma}P \quad (11)$$

2.2. Complexification-Averaging

Complexification-Averaging (CxA) studies the dynamics of the envelope of oscillation, where the dynamics is slower than the oscillations themselves, hence referred to as the Slow Flow Dynamics. This procedure will be used to obtain the Frequency Response (FR) and Slow-Invariant Manifolds (SIM)s of the oscillation envelope. Considering the case of a first-order CxA, the oscillations are assumed to have a single frequency Ω corresponding to the excitation frequency. The complex variables of Manevitch [70], A and B facilitate this procedure, and are defined as:

$$2A(\tau) \exp(j\Omega\tau) = \bar{y} - j\frac{\bar{y}'}{\Omega} \quad 2B(\tau) \exp(j\Omega\tau) = \bar{z} - j\frac{\bar{z}'}{\Omega} \quad (12)$$

where $A \in \mathbb{C}$ and $B \in \mathbb{C}$ hold the amplitude and phase modulation. The original dynamic real variables \bar{y} and \bar{z} , and its derivatives, can be obtained by:

$$\begin{aligned}\bar{y} &= A(\tau) \exp(j\Omega\tau) + A^*(\tau) \exp(-j\Omega\tau) \\ \bar{y}' &= j\Omega(A(\tau) \exp(j\Omega\tau) - A^*(\tau) \exp(-j\Omega\tau)) \\ \bar{y}'' + \Omega^2 \bar{y} &= j2\Omega A' \exp(j\Omega\tau) \\ \bar{z} &= B(\tau) \exp(j\Omega\tau) + B^*(\tau) \exp(-j\Omega\tau) \\ \bar{z}' &= j\Omega(B(\tau) \exp(j\Omega\tau) - B^*(\tau) \exp(-j\Omega\tau)) \\ \bar{z}'' + \Omega^2 \bar{z} &= j2\Omega B' \exp(j\Omega\tau)\end{aligned}\tag{13}$$

Where j is the imaginary variable and $(*)$ indicates the complex conjugate. Substituting Eq. (13) into Eq. (10) and keeping only the terms with frequency Ω yields:

$$\begin{aligned}j2\Omega A' + j\varepsilon\xi\Omega A + (1 - \Omega^2)A + \varepsilon(j2\Omega B' - \Omega^2 B + j2\Omega A' - \Omega^2 A) &= \frac{\varepsilon\bar{P}}{2} \\ j2\Omega B' + j2\Omega A' - \Omega^2 B - \Omega^2 A + j\xi_{na}\Omega B + 3B|B|^2 &= 0\end{aligned}\tag{14}$$

which is basically an averaging procedure over the forcing frequency Ω . In steady-state ($A' = B' = 0$), Eq. (14) is reduced to:

$$\begin{aligned}j\xi\sqrt{X}A + \sigma A - XB - XA &= \frac{\bar{P}}{2} \\ -XB - XA + \xi_{na}j\sqrt{X}B + 3B|B|^2 &= 0\end{aligned}\tag{15}$$

with $X = \Omega^2$ and $\varepsilon\sigma = 1 - X$. The stability of the steady-state solutions is computed using the Jacobian in Appendices A and B. Next, the complex variables A and B are defined in their amplitude-phase form as $A = \frac{a}{2} \exp(j\alpha)$ and $B = \frac{b}{2} \exp(j\beta)$, where $a, b, \alpha, \beta \in \mathbb{R}$. Therefore, the equations above can be manipulated to obtain two equations in variables $Z_a = a^2$ and $Z_b = b^2$. The second one is a SIM between the Z_a and Z_b :

$$X^2 Z_a = Z_b \left(X \xi_{na}^2 + \left(X - \frac{3}{4} Z_b \right)^2 \right)\tag{16}$$

and the first a SIM that relates Z_b with \bar{P} :

$$\left[(X - \sigma) \left(\frac{3}{4} Z_b - X \right) + X \xi_{na} \xi + X^2 \right]^2 Z_b + X \left[\xi \left(\frac{3}{4} Z_b - X \right) + (\sigma - X) \xi_{na} \right]^2 Z_b = \left(X \bar{P} \right)^2\tag{17}$$

For a given forcing level \bar{P} , a frequency response can be computed by first solving Eq. (17) for Z_b over a range of frequencies $X = \Omega^2$ and computing the corresponding Z_a from Eq. (16). The stability of the fixed points of the SIMs $Z_a - Z_b$ and $Z_b - \bar{P}$ are given in Appendix A and Appendix B respectively. The maxima and minima of the SIM (also called as fold bifurcation points) are important in tuning of the cubic stiffness coefficient. Especially the maxima, as it signifies the saturation of the host system's amplitude. These are obtained by differentiating Eq. (16) w.r.t Z_b and

finding the roots:

$$Z_b^+ = \frac{8}{9}X + \frac{4}{3\sqrt{3}}\sqrt{\frac{X^2}{3} - X\xi_{na}^2} \quad (18a)$$

$$Z_b^- = \frac{8}{9}X - \frac{4}{3\sqrt{3}}\sqrt{\frac{X^2}{3} - X\xi_{na}^2} \quad (18b)$$

$$Z_a^+ = Z_b^-\left(X\xi_{na}^2 + \left(X - \frac{3}{4}Z_b^-\right)^2\right)/X^2 \quad (18c)$$

$$Z_a^- = Z_b^+\left(X\xi_{na}^2 + \left(X - \frac{3}{4}Z_b^+\right)^2\right)/X^2 \quad (18d)$$

These points on the SIM define the limits of a quasi-periodic oscillation, as elaborated in the following section. They are also used for optimal NES tuning, as values where the response envelope saturates with increased forcing.

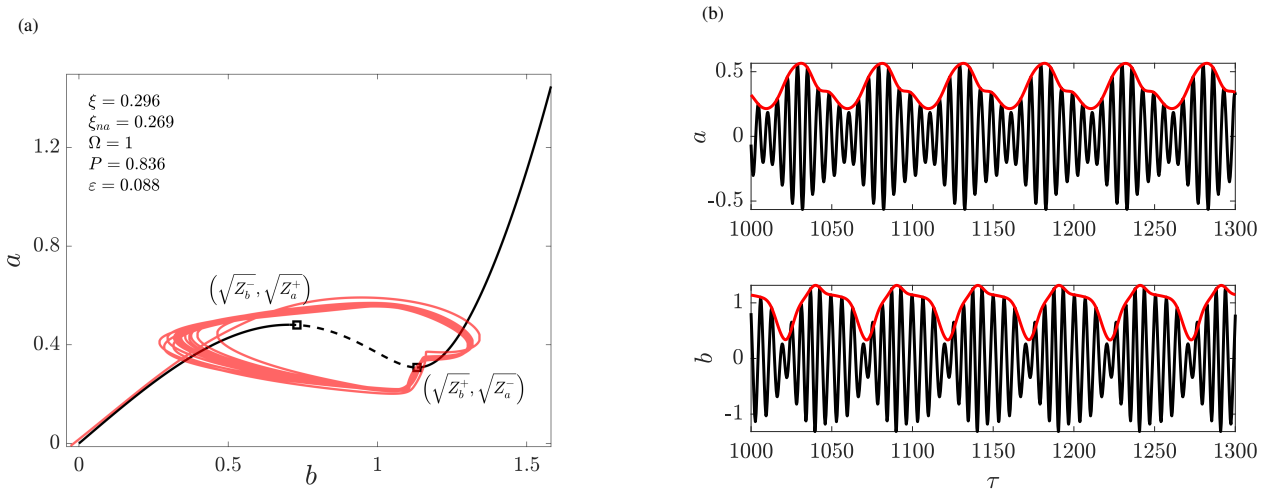


Figure 2: The Slow Invariant Manifold (SIM) and Slow Flow dynamics. (a) The SIM of Z_a and Z_b , where $a = \sqrt{Z_a}$ and $b = \sqrt{Z_b}$ represent the host response and the relative response of the Nonlinear Energy Sink (NES), respectively. The stable (black, —) and unstable (black, - - -) solutions are indicated, along with the extrema (□). The SIM is overlaid with the response envelope (light red, —) obtained from (b) time response simulations. In (b) the envelope (red, —) and oscillations (black, —) are indicated. The numerically simulated response attracts to the SIM and saturates to a quasi-periodic Strongly Modulated Response (SMR).

2.3. Explanation of Dynamical Behaviour

In this section, the dynamical behaviour of the system is explained in relation to the SIM equations calculated previously. The time simulation of the full EOMs in Eq. (3) is performed, for a given harmonic forcing frequency equal the first mode, and the oscillation is extracted. Figure 2a shows the SIM calculated from CxA, for a given forcing frequency, and is compared to the envelope extracted from time simulations, shown in Fig. 2b. The response envelope here executes a cyclic motion. Note that the parameters given in the simulation correspond to that of the optimised NES design on the identified host system, presented later in Sec. 2.5 and Sec. 4.1 respectively. The response climbs the SIM left branch until the maxima $(\sqrt{Z_b^-}, \sqrt{Z_a^+})$ is reached, and then jumps to and descends on the right branch, where a faster rate of energy dissipation is achieved [23]. The response then dissipates down the right branch until the minima $(\sqrt{Z_b^+}, \sqrt{Z_a^-})$, and jumps to the left branch, and thereafter repeats this as a limit-cycle oscillation. This relaxation

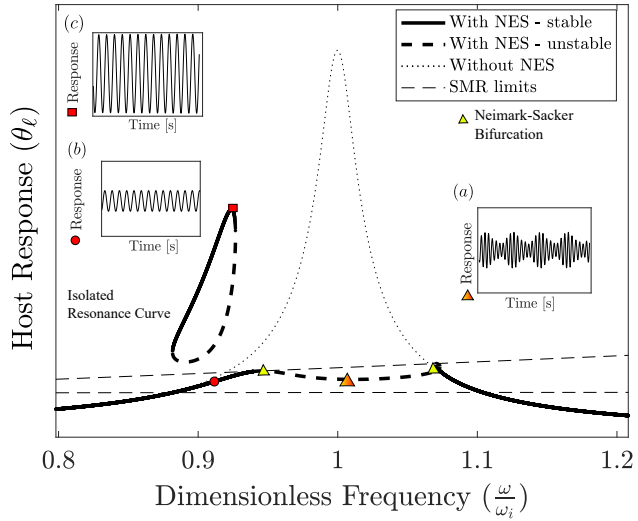


Figure 3: The frequency response of the host system with Nonlinear Energy Sink (NES) attached (stable (—) and unstable (---)) and without NES attached (···), revealing various bifurcating responses. Considering the former, the vicinity of resonance has solutions lacking linear stability, due to Neimark-Sacker bifurcations, which result in a Strongly Modulated Response (SMR) behaviour with the limits of its response envelope indicated (---); (a) the time simulation of quasi-periodic SMR is shown. An Isolated Resonance Curve arises at sub-resonant frequency, where the stable-branch time simulations on (b) the main branch and (c) detached branch are shown, where the detached branch has a higher response.

oscillation between stable branches of the SIM is referred to as the Strongly Modulated Response (SMR). The SMR effectively saturates the host structure amplitude to $\sqrt{Z_a^+}$. The SIM maxima and minima are called fold points in bifurcation theory. Furthermore, the presence of this behaviour depends on the existence of these fold points on the SIM (explained in Appendix C), and whether the forcing amplitude is sufficient to overcome the maxima of the SIM, which acts as the threshold for SMR initiation.

The SIM of the host Frequency Response (FR) (Z_a Vs. \bar{P}) is considered next, obtained from Eqs. (16) and (17). Figure 3 gives an example of the frequency response of the host, with and without the NES attached. Here, a significant reduction in the resonant response is noticeable with the NES attached. However, the stability analysis predicts that the vicinity of the resonance is an unstable solution. This instability only indicates that the envelope magnitude is not asymptotically stable as assumed ($A' = B' = 0$ in Eq. (14)), and from the time simulations it is visible that the response behaves as a quasi-periodic limit-cycle that is the SMR (refer Fig. 2b). This type of bifurcation in the FR, where the fixed points of the response envelope lose linear stability to have two pairs of complex conjugate eigenvalues, where one pair goes from a negative to a positive real part, is called Neimark-Sacker (NS) bifurcation [84]. The stability is calculated from the eigenvalues of the Jacobian in (A.4). Analysis of this bifurcation for a cubic stiffness NES is presented in a previous study by the co-author [85]. Another bifurcation is observed in the sub-resonant range, the Isolated Resonance Curve (IRC), which is a detached solution from the main branch, and has a stable solution branch with a higher amplitude than the main branch. The presence of an IRC is considered a disadvantage for the NES performance because it may attract the response, depending on the initial conditions. An IRC is often undetected in experimental testing and numerical simulation until it fully attaches, and can be catastrophic as the response can jump to the stable part of the IRC when excited by an additional input of excitation (initial conditions).

2.4. Parameter Influence

The effect of various NES parameters on the dynamical behaviour of the NES-host is studied. First, variations in the SIM and the FR are explored, then the detrimental IRC bifurcation is tracked on the FR.

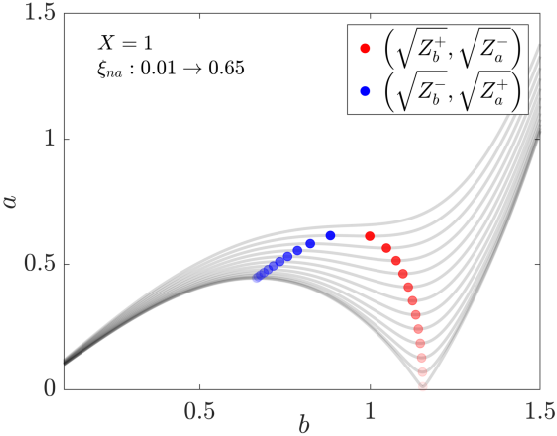


Figure 4: The influence of the Nonlinear Energy Sink (NES) damping parameter ξ_{na} on the Slow Invariant Manifold (SIM) of Z_a and Z_b , for a constant forcing frequency ratio X . Here, $a = \sqrt{Z_a}$ and $b = \sqrt{Z_b}$ are the host system displacement and relative displacement of the NES respectively. The points denoting the SIM extrema become less transparent as the damping parameter increases.

2.4.1. Variation of the SIM: Z_a and Z_b

The study of the SMR regime and the response threshold is studied from the variations in the SIM of Z_a and Z_b . Inspecting Eq. (16), it is seen that the only tunable parameter that affects the SIM is the NES damping ξ_{na} , and its influence is shown in Fig. 4, for a given forcing frequency. As the NES damping ξ_{na} increases, the minima increases on a while decreasing on b , and the maxima increases on both a and b . This implies that with an increase in damping, the extrema converge to a point and vanish altogether, eliminating the potential for SMR behaviour. This is in accordance with the bifurcation condition presented in section Appendix C, where this threshold on ξ_{na} is also derived. Additionally, the increase of Z_a^- is more pronounced than that of Z_a^+ , implying a less pronounced or "deep" SMR oscillation in the host system response. A higher SIM maxima also implies an increase of the vibration threshold to initiate SMR and a decrease in NES vibration attenuation.

Based on the above analysis, a lower ξ_{na} is considered advantageous, as it can be used to lower the threshold for SMR initiation and enhance NES performance.

2.4.2. Variation of the frequency response: Z_a and \bar{P}

The parameter influences on the FR is considered for different forcing levels (\bar{P}) and for different NES damping ξ_{na} . The FR obtained from Eqs. (16) and (17) is shown for various forcing levels (\bar{P}) and for dimensionless NES damping ξ_{na} in Fig. 5. As dimensionless forcing increases from $\bar{P} = 0.71$ to $\bar{P} = 0.96$ for $\xi_{\text{na}} = 0.269$, in the vicinity of the resonant frequency of the host, a saturation in the response amplitude is observed in Fig. 5a. This is indicative of the SMR regime, as explained by the SIM of Z_a and Z_b in Section 2.3, and is attributed to a NS bifurcation in the FR. The modulation in the response envelope is dictated by the extrema of the SIM, defined by Eqs. (18c) and (18d) and is plotted as thin dashed lines, where the maximum response is the maxima of the SIM (Eq. (18c)). As a consequence, the resonant response attenuation increases from 80% to 85% across this forcing range, considering the

maxima of the saturated response and the resonant response of the unattenuated host. As such, this serves as a design criterion for suppressing response to safe levels. If the host response stays below the maxima due to low forcing amplitudes, then NS bifurcation is absent and the absorber is not activated. Therefore, the SIM limits should also be calculated taking the forcing capacity/limit of the host into account. The increase in dimensionless forcing also results in the inception and enlargement of a sub-resonant IRC, until it merges with the main resonance curve. It should be noted the peak of the attached IRC is lower than the resonance peak of the unattenuated host. The parameter values corresponding to IRC inception and merging are discussed in detail in the following section.

When the NES damping increases from $\xi_{na} = 0.269$ to $\xi_{na} = 0.46$ for $\bar{P} = 0.96$ (Fig. 5b), the maxima (Z_a^+) of the saturated response increases, and the frequency range of SMR is diminished, as seen by the decreasing frequency range of unstable solutions around 1:1 resonance. This is in accordance with the SIM parameter study in Section 2.4.1. The attenuation performance of the NES decreases from 85% to 83% across the damping range, considering the maxima of the saturated response and the resonant response of the unattenuated host. The extent of the IRC is also controlled, ranging from being attached to the main branch to inexistence as NES damping increases. A detailed study of the IRC follows next.

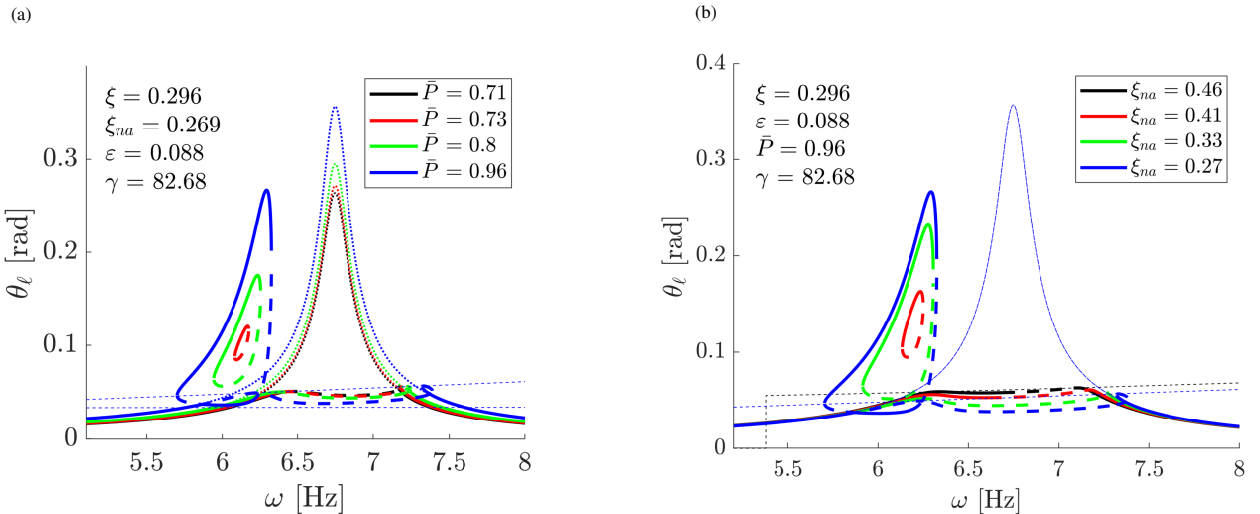


Figure 5: Frequency response (FR)s of the host system with the Nonlinear Energy Sink (NES) attached (stable (—) and unstable (---) solutions) compared to that of the host system without NES (···), for (a) variations in the forcing level \bar{P} and (b) variation in the NES damping ξ_{na} . A Strongly Modulated Response (SMR) regime is observed in the vicinity of the 1:1 resonance and indicated by unstable solutions. The extent of the SMR is defined by the extrema of the Slow Invariant Manifold (SIM) of Z_a and Z_b (---). In (a) the SIM extrema are unaffected by \bar{P} . In (b) the SIM extrema is influenced by ξ_{na} , and the maxima of the SIM for $\xi_{na} = 0.46$ and $\xi_{na} = 0.27$ is indicated by (black, - - -) and (blue, - - -) respectively.

2.4.3. Tracking Isolated Response Curves

The behaviour of the IRC bifurcation is analysed using Singularity theory [86], which tracks the bifurcation based on the nature of the inflection points of the FR curve. The dimensionless forcing \bar{P} , dimensionless NES damping ξ_{na} , and dimensionless forcing frequency Ω are considered the bifurcation parameters. The parameter values at which the IRC appears and merges with the main resonance curve are computed and shown in Fig. 6 below. The results given here serve as a validation for the FR parametric analysis presented in Sec. 2.4.2.

First, the parameter combinations causing the IRC appearance are tackled in Fig. 6a. Here, as ξ_{na} increases, the forcing threshold of \bar{P} for IRC appearance (or inception) also increases. This increase follows a linear trend until

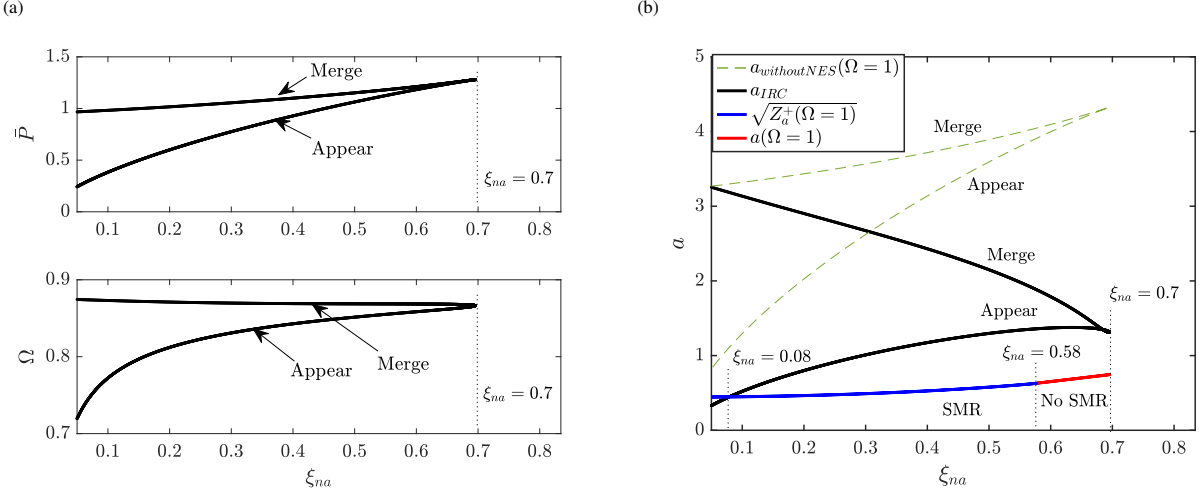


Figure 6: Analysis of Isolated Resonance Curve (IRC); (a) Bifurcation diagram showing the dimensionless forcing \bar{P} and dimensionless frequency Ω where the IRC appears and touches the main resonance curve and (b) the host response at which the IRC appears and merges is compared to the host resonant response with and without NES, for the forcing levels at which the IRC appears and merges. The analysis is performed for $\varepsilon = 0.088$ and $\xi = 0.296$.

$\xi_{na} = 0.7$, which forms the threshold after which the IRC is no longer formed. Additionally, the IRC always appears in the sub-resonant frequency domain and the corresponding Ω varies from 0.7 to approaching 0.86 as the NES damping ξ_{na} increases till the threshold. For the case where IRC merges, at low ξ_{na} there is a significant difference between the forcing threshold for IRC appearance and merging, the thresholds increase with damping and approach each other. In particular, the IRC merging is also sub-resonant, at $\Omega \approx 0.86$ irrespective of the NES damping. This suggests that regarding IRCs, a larger ξ_{na} is beneficial. However, in section 2.4.1 it was argued that a lower ξ_{na} is desirable for lowering the threshold amplitude.

Next, the host response at the IRC is compared to the resonant response in Fig. 6b. The response of the host on the IRC branch a_{IRC} is divided into corresponding values for the appeared and the merged IRC. Both responses are vastly different at low NES damping and approach each other with an increase in NES damping, indicating that the IRC begins to appear closer to the main resonance branch. For the attenuated response (with NES attached), comparing the IRC response with the response at host resonance, we see that the SIM maxima $\sqrt{Z_a^+(\Omega = 1)}$ is below the merged IRC response, except for $\xi_{na} < 0.08$, where the SIM maxima is higher. Note that the SMR at $\Omega = 1$ doesn't exist for $\xi_{na} > 0.58$ (refer Appendix C). Beyond this threshold, two branches of solutions for the host response $a(\Omega = 1)$ exist, corresponding to the appear and merge forcing threshold, but are extremely close to each other. Even in this case, the IRC response is higher. Next, the unattenuated host response at resonance $a_{\text{withoutNES}}(\Omega = 1)$, for both appear and merge forcing threshold, is compared to the IRC response. At low NES damping, the difference between the responses is less pronounced, with the merged branch having almost the same magnitude as the unattenuated host at very low NES damping. This margin between them increases with NES damping, with the unattenuated host having a higher response, therefore mitigating, to an extent, the detrimental effect of an IRC. Here, lower ξ_{na} seems beneficial as it lowers the IRC appear amplitude, the amplitude $\sqrt{Z_a^+(\Omega = 1)}$ and ensures SMR.

The detailed parameter analysis presented in the sections above serves to provide insights for NES tuning, which is covered next.

2.5. Insights for tuning

The first step in the NES tuning is to find the optimal dimensionless NES parameters. In line with the main objective of the NES, saturation of the host resonant response via the SMR is desired for the range of forcing provided by the host. First, the host system needs to be identified (refer Section 4.1) and its forcing levels (F_1) quantified. A series of initial guesses can be used for the NES parameters. The NES inertia is considered to be significantly lower than the host inertia, resulting in the parameter $\varepsilon \ll 1$. Care should be taken that the resulting diameter of the NES inertia I_{na} is feasible for the implementation of the design. Next, we tackle the parameters ξ_{na} and γ .

To ensure the possibility of SMR at host resonance ($X = 1$), $\xi_{na} < 0.577$ is required (refer Appendix C), and from Section 2.4.1 it is shown that decreasing ξ_{na} and thereby c_{na} implies a lower host response saturation Z_a^+ , and a value is chosen so that the response is suppressed to safe levels. To trigger SMR, the limits of host forcing are amplified with the nonlinearity parameter γ , and thereby k_{na} , to obtain \bar{P} . This would in turn provide values for Z_b and Z_a from Eqs. (16) and (17). Therefore γ is adjusted such that the $Z_a > Z_a^+$ at $X = 1$ for the forcing limits of the host, and ensures SMR at resonance; the saturation amplitude is not affected here. Both γ and ξ_{na} are chosen such that SMR is triggered, and the response is within the safe levels of the machinery.

The sub-resonant IRC can also be considered in the tuning. The tuning to avoid the IRC behaviour is nuanced. From Fig.6, for low ξ_{na} , the IRC appears for lower forcing \bar{P} , and the response amplitude a at appearance is quite low. Furthermore, the saturation amplitude ($\sqrt{Z_a^+}$) is also lower for low ξ_{na} . An exception is for $\xi_{na} < 0.08$ where the SMR response has a higher saturation amplitude than at the IRC. On the other hand, a higher ξ_{na} allows for higher forcing \bar{P} without IRC, yet the amplitude of saturation and at the IRC is higher. If ξ_{na} is to be within the limit $\xi_{na} < 0.7$, then γ needs to be chosen such that forcing limits on \bar{P} doesn't trigger an IRC appearance; $\xi_{na} > 0.58$ also loses the SMR response meaning that the resonant response can increase with the forcing levels. However, if $\xi_{na} > 0.7$ then IRC is never triggered for any forcing level, but the SMR regime is absent at resonance. A trade-off in the resonant response attenuation (due to an increase in saturation amplitude) might be necessary for mitigating the IRCs. The objective of tuning to avoid IRCs is not considered here, as the experiment intends to showcase the different nonlinear bifurcating behaviour possible.

The host system that will be used in the experiment, shown in Fig. 7a, is a 2-DOF system with the NES attached to inertia I_2 , and its identification is mentioned in detail in Section 4.1. Here, the tuning of the NES is meant to attenuate the first mode of the host ($i = 1$ in Eq.(7)). As the primary objective is to showcase the bifurcations, a low ξ_{na} is chosen, such that resonant SMR and the sub-resonant IRC are easily triggered. A starting value of $\xi_{na} \ll 1$ (≈ 0.1) is chosen, as the design presented in the following sections doesn't have a specific damping mechanism implemented. Then, a value of k_{na} (and thereby γ) is chosen so that SMR and IRC are triggered for the forcing levels of the host, with a small margin intended for errors in ξ_{na} . The threshold forcing levels are obtained based on the identified parameters of the host in Eq. (31). The NES damping is later identified from experiment (refer to Section 4.2), and then the actual forcing limits are estimated. Finally, a value of $k_{na} = 110 \text{ N rad}^{-3}$ is chosen and $c_{na} = 0.0085 \text{ N rad}^{-1}\text{s}^{-1}$ is identified. The NES inertia is optimised to be as minimal as possible, and for the experimental setup $I_{na}=7.4\text{e-}04 \text{ Kg m}^2$. The parameters are chosen so that they allow the NES to exhibit its typical behaviour of SMR and IRC within the force range that the benchmark system can provide.

3. Design Methodology

In the previous section, analytical calculations were used to obtain an optimal NES stiffness curve. The following section is dedicated to realising this. A description of the underlying mechanism of the piecewise-stiffening NES is

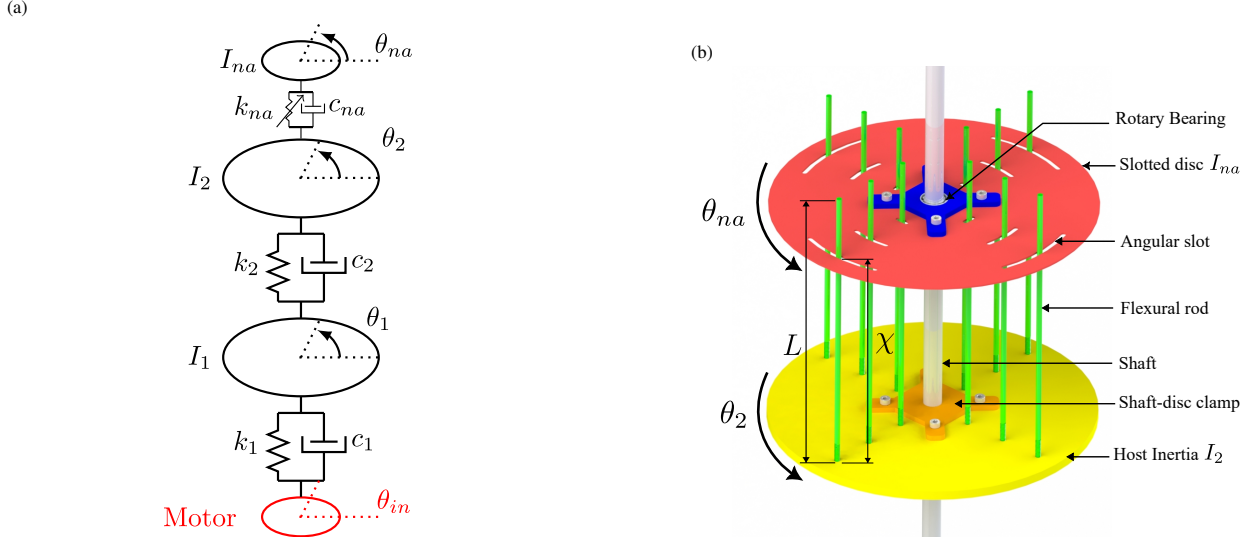


Figure 7: The dynamical model of the benchmark host system with NES attached and the concept of a piecewise-stiffening Nonlinear Energy Sink (NES). (a) The 2-DOF host system for validation, with the NES attached to I_2 inertia, and (b) a conceptual modal of a piecewise-stiffening NES with a slotted disc forming the inertia I_{na} and a piecewise-linear stiffness obtained by engagement of flexural rods on angular slots at different intervals. The rods are attached to host inertia I_2 , which is clamped to the shaft. The slotted disc of the NES inertia is free to rotate about the shaft, and engages with the rods of length L at a distance χ from I_2 .

presented, followed by calculations of local stresses, fatigue, and resonance conditions for individual components. Lastly, a design optimisation problem is formulated that incorporates all the above aspects, resulting in a reliable and optimally tuned NES design.

3.1. Conceptual design and piecewise approximation of nonlinearity

The concept of a piecewise-stiffening NES is to approximate a nonlinear stiffness profile via a combination of piecewise-linear segments [76]. In this regard, the preliminary design is presented in Figs. 7b (conceptual CAD) and 11d (Experimental) with a top-down view schematic in Fig. 11c; the last two figures are for the optimised design presented in the following subsection. Here, the NES inertia I_{na} is a slotted disc that can rotate freely on the shaft via a rotary bearing. Flexural rods are attached to the host inertia I_2 and they engage with the angular slots of the slotted NES disc. The Inertia I_2 is rigidly connected to the shaft using a clamping mechanism, and the imposed motor motion will thus oscillate this inertia. As the oscillation amplitude increases, more number of flexural rods engage with the angular slots of the NES. The piecewise-linear torsional stiffness is created by the engagement of these flexural rods with the angular slots, which are of different angular intervals on the slotted disc. The slots and rod dimensions are chosen according to the nonlinear profile to be approximated. The piecewise-linear stiffness thus obtained is shown in Fig. 8a. Furthermore, several rods can engage in parallel at the same angle and contribute to the stiffness, as seen in Fig. 7b, and this reduces the stiffness contribution required of each individual rod.

Consider a rod made of a material having elastic modulus E , density ρ , where each rod, indicated by subscript h , has a diameter d_h and length L . Each of them engages with its corresponding slot on the NES inertia at a radial distance of R_h only if the relative angle between the NES and the host disk ($z = \theta_{na} - \theta_2$) is larger than its slot angle ϑ_h , as seen in Fig. 8b. This engagement occurs at a distance χ from inertia I_2 (refer Fig. 7b). Once engaged, the rod undergoes an angular deflection of $\delta\vartheta_h = |z| - \vartheta_h$, and therefore a linear deflection of $\delta\vartheta_h R_h$, assuming the angular

deflection to be small. The tangential force due to this linear deflection is written as:

$$F_t = \frac{6EI}{\chi^2(3L-\chi)} R_h (|z| - \vartheta_h) \quad (19)$$

Where $I = \frac{\pi d_h^4}{64}$ is the moment of inertia of the rod. The restoring torque $T_h = R_h F_t$ obtained from a single rod is as follows:

$$T_h = \underbrace{\frac{6EI}{\chi^2(3L-\chi)} R_h^2}_{k_{\vartheta,h}} (|z| - \vartheta_h) \quad (20)$$

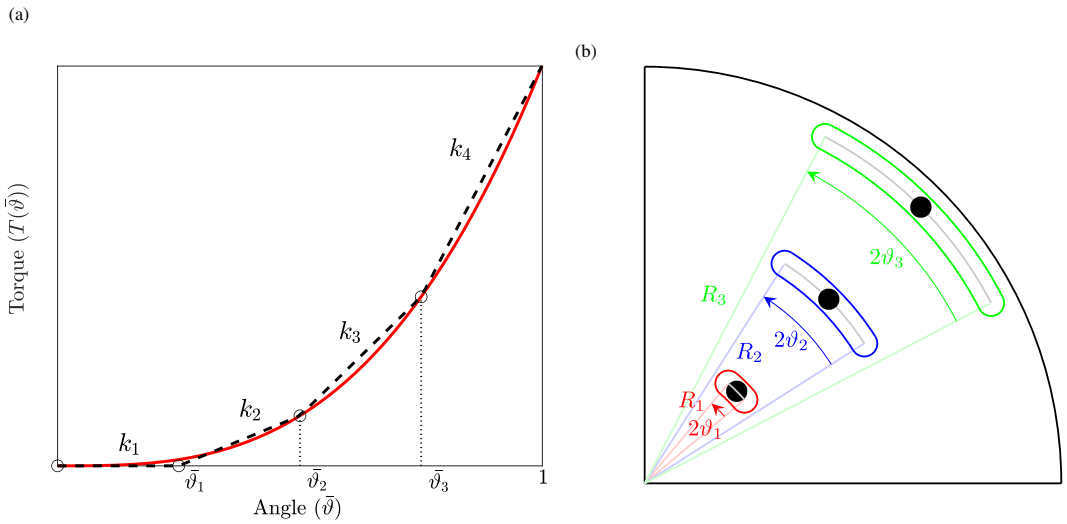


Figure 8: The piecewise-linear stiffness concept with four stiffness increments. (a) Piecewise-linear approximation (black, (—)) compared to the cubic nonlinearity (red, (—)). Note that $\bar{\vartheta} = \frac{\vartheta}{\vartheta_{max}}$ where ϑ is the relative angular displacement of the NES and ϑ_{max} is the maximum allowable displacement. The Torque-Angle curve is symmetric about the origin with $T(-\bar{\vartheta}) = -T(\bar{\vartheta})$. (b) The parameters of the piecewise linearity; angular slots of $2\vartheta_h$ are located at a radial distance R_h , interfacing with the corresponding rod of index h .

Where $k_{\vartheta,h}$ is the torsional stiffness. The piecewise-linear stiffness function from multiple rod engagements can be written as in Eq. (21). In this article, the nonlinear stiffness is approximated in four stiffness increments.

$$k_{\vartheta}(z) = \begin{cases} k_{\vartheta,1} & (|z| \leq \vartheta_1) \\ k_{\vartheta,1} + k_{\vartheta,2} & (\vartheta_1 < |z| \leq \vartheta_2) \\ k_{\vartheta,1} + k_{\vartheta,2} + k_{\vartheta,3} & (\vartheta_2 < |z| \leq \vartheta_3) \\ k_{\vartheta,1} + k_{\vartheta,2} + k_{\vartheta,3} + k_{\vartheta,4} & (\vartheta_3 < |z| \leq z_{max}) \end{cases} \quad (21)$$

Where z_{max} ($= \vartheta_{max}$, in Fig. 8) is the maximum displacement that will be considered in the design. Note that if multiple rods engage within the same interval, the stiffness increments above should be multiplied by the number of simultaneous engagements. Additionally, the stiffness of each rod $k_{\vartheta,h}$ is defined according to the nonlinear stiffness function $F_{na}(z) = k_{na,h}z^3$ as shown in Eq. (22) below. Here, $k_{na,h} = \frac{k_{na}}{n_p}$ is the stiffness contribution of a single rod, where n_p is the number of parallel rods engaging for the same stiffness interval in k_{ϑ} (see Fig. 7b). A comparison of the cubic nonlinear stiffness and the approximated piecewise-linear stiffness is shown in Fig. 8a. Note that the

stiffness function is symmetric about the origin.

$$k_{\theta,h} = \frac{k_{na,h}\vartheta_h^3 - \sum_{i=1}^{h-1} (k_{\theta,i}(\vartheta_h - \vartheta_{i-1}))}{\vartheta_h - \vartheta_{h-1}} \quad 1 \leq h \leq 4 \quad (22)$$

where $\vartheta_0 = 0$, $\vartheta_4 = \vartheta_{max} = z_{max}$

For the design implemented in the article, the chosen non-linear stiffness profile with coefficient $k_{na} = 110 \text{ N/m}^3$ is approximated with 4 piecewise-linear segments of equal angle increments $\Delta\vartheta_h = 0.025 \text{ rad}$ and $n_p = 3$ number of parallel engagements, until the maxima allowable angle $\vartheta_{max} = 0.1 \text{ rad}$. The individual stiffness contributions of the rods ($k_{\theta,h}$) are given in Eq. (23) below. Note that $k_{\theta,1} = 0$ is a choice for the design.

$$k_{\theta,1} = 0 \text{ N/m} \quad k_{\theta,2} = 0.183 \text{ N/m} \quad k_{\theta,3} = 0.252 \text{ N/m} \quad k_{\theta,4} = 0.412 \text{ N/m} \quad (23)$$

3.2. Material stress and local resonance

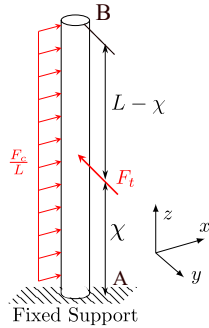


Figure 9: Forces acting on a flexural rod attached to the host inertia I_2 , represented as a fixed support. A tangential point-load F_t from the torque due to deflection acts at a location χ from the fixed support. A uniformly distributed load F_c from centrifugal force acts along the length of the rod, due to the rotation of the fixed support, i.e., inertia I_2 .

A major drawback of the cubic nonlinearity is its need to sustain large displacements (above the maxima of the SIM as in Fig. 2a) to attain the SMR regime. This tends to induce high stresses, making individual components prone to yielding and vibration-induced fatigue failure. Fatigue study is even more relevant because of the cyclical nature of SMR. Furthermore, to ensure that the assumed stiffness is correct when rods are engaged, the design should also avoid local resonance of the rods. This is because Eq. (20) assumes that the eigenfrequencies of the rod are distant from the rotational frequency of the system, thus allowing for expressions of static deflection in calculating stiffness.

Each rod engages with its corresponding slot at a radial distance of R_h at intervals ϑ_h and undergoes deflection. Additionally, z_{max} is the maximum deflection allowed in the design, where $\vartheta_{2,max} \approx z_{max}$ imitates a stationary NES inertia. Then each flexural rod of the NES is subjected to two main forces; (1) a tangential force F_t , which is a point load due to the torque located at a distance χ from the fixed support of the rod, caused by the angular deflection of the rod by the slotted disc (NES inertia), and (2) a centrifugal force F_c acting as a uniformly distributed load along the length of the rod, caused by the angular speed of the rotating shaft compounded with the relative angular speed of the rods. The forces are visualised in Fig. 9.

$$F_c = \underbrace{\rho \frac{\pi d_h^2}{4} L R_h}_{m_h} (\theta_{2,max} \omega_{max})^2 \quad (24)$$

$$F_t = \frac{6E \pi d_h^4}{\chi^2 (3L - \chi) 64} R_h (\theta_{2,max} - \vartheta_h)$$

Here, F_c is calculated for a given rod of mass m_h at its highest possible magnitude of angular velocity $\theta_{2,max} \omega_{max}$, and F_t is defined as $\frac{T_h}{R_h}$. The bending moment and thus, the bending stress would be maximum at A (refer to Fig. 9) and is given by Eq. (25). The stresses can be minimised by decreasing R_h , d_h , E and by increasing $\chi (\leq L)$.

$$\sigma_{max,h} = \frac{32 \left(\sqrt{(\chi F_t)^2 + \left(\frac{F_c L}{2} \right)^2} \right)}{\pi d_h^3} \quad (25)$$

For analysing local resonances of the flexural rods, a sufficiently accurate estimation of the first eigenfrequency of the rod can be obtained using the Rayleigh Quotient method. This assumes that the rod's response mimics its static displacement. For this to hold, it should be avoided that the rods themselves are excited near their natural frequency. The modal response of a rod h is defined as $\bar{y}_{h,p}(\bar{x}_h, t)$ along its length \bar{x}_h is defined for a mode p , as in Eq. (26).

$$\bar{y}_{h,p}(\bar{x}, t) = \psi_p(\bar{x}_h) \phi_p(t) = \psi_p(\bar{x}_h) \sin(\gamma_{p,h} t + \alpha_p) \quad (26)$$

For the 1st mode ($p = 1$), the assumed spatial eigenfunction $\psi_1(\bar{x}_h)$ is defined in Eq. (27).

$$\psi_1(u) = \frac{1}{2} (3u^2 - u^3), \quad u = \frac{\bar{x}_h}{L}; \quad 0 \leq u \leq 1 \quad (27)$$

The first eigenfrequency $\gamma_{1,h}$, mentioned hereafter as γ_h , is critical for design. Here, the trial eigenfunction $\psi_1(u)$ is approximated as the static deflection of the rod. The Rayleigh-Ritz reduction is performed to obtain the equivalent mass and stiffness of the rod, which provides the natural frequency of the rod. The computation for the Rayleigh Coefficient R is shown below:

$$R(\psi_1(u)) = \gamma_h^2 = \frac{\int_0^1 EI(\ddot{\psi}_1)^2(u) du}{\int_0^1 \rho A \psi_1^2(u) du} = \frac{k_{h,eq}}{m_{h,eq}} = \frac{35}{44} \frac{d_h^2 E}{\rho L^4} \quad (28)$$

Where $(\ddot{\cdot}) = \frac{d^2(\cdot)}{du^2}$, and $f_{1,h} = \frac{\gamma_{1,h}}{2\pi}$ [Hz] is the natural frequency of a flexural rod. Thus, a discrete 1-DOF equation of motion for the rod is obtained as follows:

$$\ddot{q}_h + 2\zeta_h \gamma_h \dot{q}_h + \gamma_h^2 q_h = f_h \cos(\omega t) \quad (29)$$

Where ζ_h , γ_h , and f_h are the damping factor, the natural frequency, and the modal forcing amplitude of the rod, respectively. The rod is considered lightly damped (damping factor $\zeta_h \approx 0.01$ [87]) and the forcing is harmonic in nature. The frequency response and dynamic stiffness of the rod is obtained in Fig. 10 below, and made dimensionless by scaling with the unit-force static response ($q_{h,stat} = \frac{1}{k_{h,eq}}$). The plots show that as the forcing frequency approaches the rod's resonance, there is an increase in rod vibrations and a corresponding decrease in stiffness. The analysis here helps to assign a limit on the forcing frequency where the rod dynamics can be neglected. For optimal NES perfor-

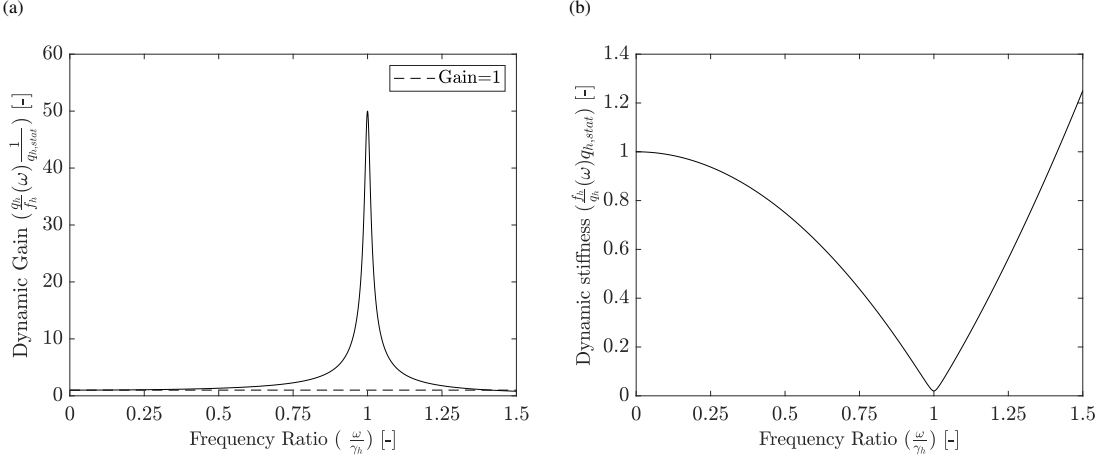


Figure 10: Response of the flexural rod to harmonic forcing. (a) The frequency response and (b) the dynamic stiffness of a rod, made dimensionless with the unit-force static displacement $q_{h,stat}$. The rod is considered to be lightly damped with damping ratio $\zeta_h = 0.01$.

mance, apart from the maximum excitation frequency of the host, the host resonant frequency is a more important factor that must be far below the resonance of the rods.

3.3. Design optimisation

A general design optimisation procedure is developed with the principal idea of minimizing the bending stress in the rods and avoiding local resonances, while maintaining the stiffness profile as desired. The design variables are the diameters of the rods and their length, and therefore Eqs. (20), (25) and (28) are parametrized with these variables. Note that $\chi = L$ is chosen, with the intention of minimizing the rod stress. Additionally, based on the host system's requirements and limitations, certain constraints are placed on the absorber dimensions. With these under consideration, we can formulate an optimisation problem as follows:

$$\begin{aligned}
 & \text{minimize} && \sigma_{max,h}(d_h, L) \\
 & \text{subject to} && f_{1,h}(d_h, L) \geq \lambda f_1 \\
 & && d_{h,min} \leq d_h \leq d_{h,max} \\
 & && L_{min} \leq L \leq L_{max} \\
 & && R_{h,min} \leq R_h \leq R_{h,max}
 \end{aligned} \tag{30}$$

The objective function to minimise is the maximum bending stress of the rods (see Eq. (25)). The constraints of the optimisation are elaborated next. The first constraint restricts the natural frequency of the rod $f_{1,h}$ to be equal to or greater than λ times the resonant frequency of the host f_1 . This parameter defines the degree to which the rod dynamics can be neglected, and a larger value is favourable. In this case, $\lambda = 5.56$ is chosen, and from Fig. 10, this places the frequency ratio at the host resonance $\frac{\omega_1}{\gamma_h} < 0.18$ for all the rods; the loss of stiffness due to rod dynamics and the deviation from the static response is $< 3.5\%$ for all the rods. Note that in the non-resonant frequency domain, the NES is not activated. The second constraint restricts the overall dimensions of the NES for design feasibility within the current setup.

A visualisation of the design space from the above constraints is shown in Fig. 11b. Here, the objective function is

Design Constants		Design Constants		Design Constraints	
Parameter	Value	Parameter	Value	Parameter	Limits
E [N/m]	2.06e11	ρ [Kg/m ³]	8050	d_h [mm]	ϵ [3, 12]
z_{max} [rad]	0.1	λ	5.56	L [mm]	ϵ [50, 250]
$k_{\theta,1}$ [N/m]	0	$k_{\theta,3}$ [N/m]	0.252	R_h [mm]	ϵ [29, 100]
$k_{\theta,2}$ [N/m]	0.183	$k_{\theta,4}$ [N/m]	0.412		
f_1 [Hz]	6.75				

Table 1: Design constants and constraints of the optimisation

represented as a function of the constraint variables, L and R_h ; corresponding to the rods of a $k_{\theta,h}$ stiffness increment. The black dashed lines show the constraints on L and R_h , and the red dashed lines indicate the natural frequency constraint, with arrows indicating the feasible direction. Lines of constant diameter d_h are also plotted, and can be used to indicate the corresponding constraint function. Before performing a numerical optimisation, it is recommended to have an understanding of the effect of the design variables on the objective function. The relative importance of each constraint function can be assessed by its corresponding reduction of the design space, and necessary modifications can be made to its limits.

Apart from design constraints, some design constants have also been considered as in Tab. 1. From Eq. (23), the stiffness contribution of each rod h is given as an input, considering the number of parallel engagements $n_p = 3$. The number of engagements (i.e. rods) per stiffness increment can be increased to further lower local stresses and this can be used to avoid infeasible designs. Spring steel (50CrV4) is chosen as the material for the rod as it possesses a high yield and endurance limit. The maximum rotation of $\theta_{2,max}$ is limited by the motor of the setup. Note that the limits on d_h are from manufacturing concerns, while for L and R_h , they are from the dimensional constraints of the machine.

Rod Index (h)	d_h [mm]	L [mm]	R_h [mm]	$\sigma_{max,h}$ [MPa]	$f_{1,h}$ [Hz]
1	-	-	-	-	-
2	3.2	248	29.6	36.64	37.36
3	3.4	"	30.8	27.06	36.39
4	3.8	"	31.5	16.15	44.36

Table 2: Optimised design variables, their corresponding objective function, and frequency constraint values.

Numerical optimisation is performed in MATLAB using the *fmincon* function, and the default interior-point algorithm is used. The optimisation is computationally inexpensive and allows quick convergence; the results are presented in Tab. 2. Since the available rod diameters are increments of 0.1 mm the results have been rounded accordingly. Additionally, a sensitivity analysis of the flexural rod stiffness, and the maximum bending stress of the rod is presented for the chosen design in Appendix D. The results here indicate that the rod diameter d_h has the most impact on rod stiffness and its maximum bending stress, followed by the radial slot distance R_h , but about 20 times less significant. Therefore tighter manufacturing controls should be kept on the rod diameter. The optimal design obtained has significantly lower rod stress than the material endurance limit (~ 600 MPa for 50CrV4 [88]), thus theoretically guaranteeing infinite life for the design. This assumption is valid as the stress amplitude calculated is for the highest possible deflection in the rods, and therefore stress amplitude of all other cycles is below this limit. Note that the endurance limit for bending is used as the rods are stressed under bending, and not torsion. For materials that do not possess an endurance limit, the usage of cumulative damage models (e.g. Miner's Rule) [89] is recommended

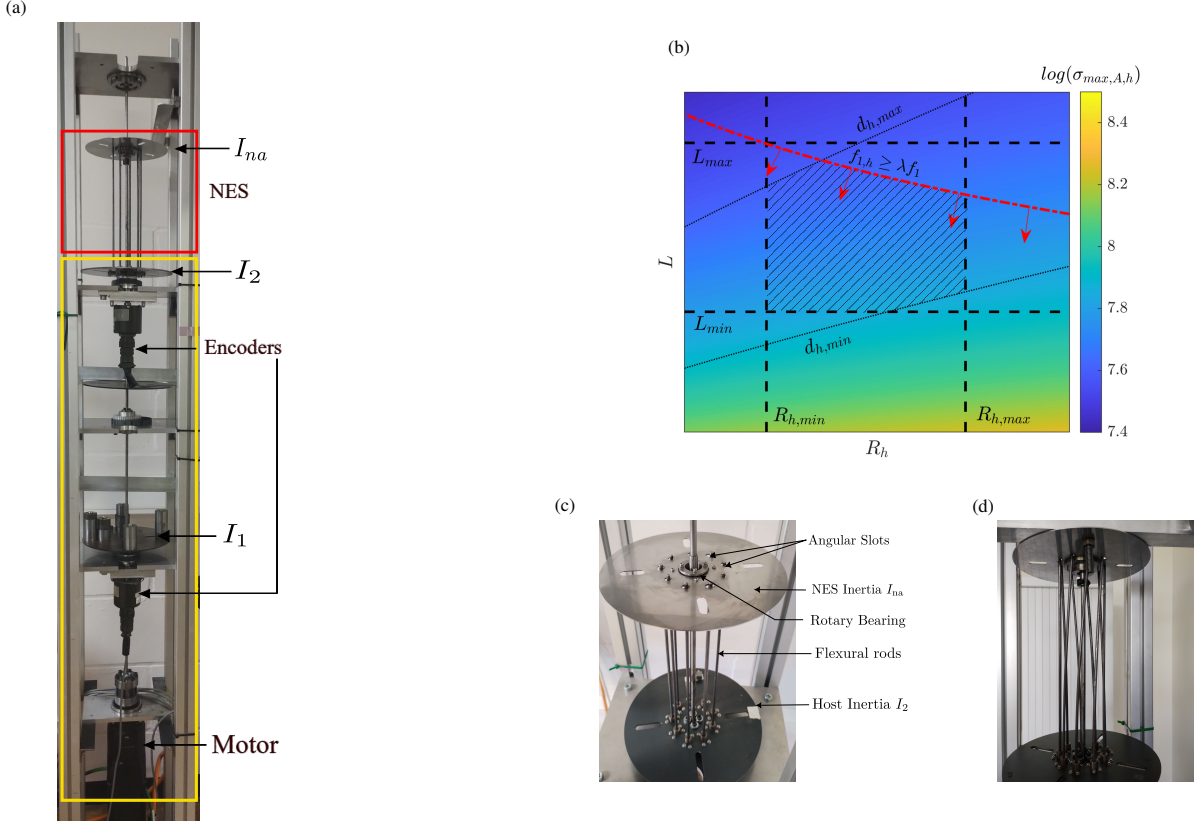


Figure 11: The optimised Nonlinear Energy Sink (NES) assembled to the host structure for experimental validation, and the optimisation problem visualised. (a) The 2-DOF benchmark system with the NES attached to inertia I_2 . (b) A visualisation of the constrained design space with the objective function indicated by the colour contours; the hatched region represents the feasible parameter zone. (c) The assembly of the NES with optimal parameters, and (d) the flexural rods bending under NES rotation.

to calculate life until failure. Since the rod deflection is expected to be maximum at resonance, the stress amplitude calculated in the analysis prior can be used with the resonant frequency to determine the number of cycles till failure. The optimised design thus obtained has been further designed in detail for implementation, as seen in Figs. 11a and 11c. The NES under rotation is also presented in Fig. 11d.

3.4. Summary of the tuning and design methodology

A brief summary of the entire design process is presented, from the tuning to the optimisation procedure. For the tuning of the NES, the parameters are listed in Tab. 3, where the dimensional parameters of the NES-host and derived parameters required for the dimensionless analysis and the range of values used in the simulation are also presented. Here, the user provides the complete information about the host system through the matrices \mathbf{M} , \mathbf{C} , \mathbf{K} and \mathbf{F} , and also the location of attachment of the NES via the vector δ_ℓ . The tuning then proceeds with the deriving dimensionless parameters, which are chosen based on the analysis from section 2.5; the NES parameters I_{na} , k_{na} and c_{na} are chosen.

At the stage of component design, the first step is to approximate the tuned cubic stiffness profile (with coefficient k_{na}) with piecewise-linear segments; the parameters are given in Tab. 4. Practical restrictions are applied here; the number of piecewise-linear segments (= 4 in the current design) and their increment angles $\Delta\theta_h$, number of parallel contributions n_p , and the maximum allowable relative displacement of the design z_{max} form the main constraints.

Dimensional parameters					
n-DOF Host Parameters			NES Parameters		
Symbol	Description	Unit	Symbol	Description	Unit
$\mathbf{I}_{(n \times n)}$	Inertia matrix	kg.m ²	I_{na}	NES inertia	kg.m ²
$\mathbf{K}_{(n \times n)}$	Stiffness matrix	Nm ⁻¹	k_{na}	cubic stiffness coefficient	Nm ⁻³
$\mathbf{C}_{(n \times n)}$	Damping matrix	N.s m ⁻¹	c_{na}	linear damping coefficient	N.s m ⁻¹
$\mathbf{F}_{(n \times 1)}$	Force vector	N			
δ_ℓ ($n \times 1$)	NES connection vector (boolean)	-			
Derived parameters					
Symbol	Description	Unit	Symbol	Description	Unit
ω_i	i^{th} natural frequency	rad/s	γ	Dimensionless NES stiffness coefficient	-
e_i	i^{th} modal vector	-	ξ_{na}	Dimensionless NES damping coefficient	-
$O_{q,i}$	i^{th} modal coefficients	-	ε	Ratio of NES inertia to modal inertia	-
ξ	Dimensionless damping coefficient	-	\bar{P}	Dimensionless forcing	-
Ω	Ratio of forcing frequency to the i^{th} natural frequency	-			
Common Values (Mode $i = 1$)					
Parameter	value		Parameter	value	
ε	0.05-0.1		ξ	0.1-0.3	
ξ_{na}	0.01-0.5		γ	37-150	
\bar{P}	0.71-0.96				

Table 3: Parameters for NES tuning. The first set contains dimensional parameters and the latter set consists of derived quantities for use in dimensionless analysis of the NES-host system. The range of parameter values used in the dimensionless analysis for the first host mode is also presented.

Piecewise-linear stiffness parameters					
Symbol	Description	Unit	Symbol	Description	Unit
h	Stiffness increment index (or rod index)	-	z_{max}	Maximum allowable angular displacement	rad
n_p	Number of parallel contributions to a stiffness increment	-	$k_{\theta,h}$	Stiffness of the h^{th} increment	N rad ⁻¹
$\Delta\theta_h$	Angle between stiffness increments	rad	-	-	-

Table 4: Parameters for fitting piecewise-linear stiffness increments on a chosen cubic nonlinear stiffness.

These parameters allow the computation of the individual stiffness contributions ($k_{\theta,h}$). The parameters here are not explicitly part of the design optimisation, but can be adjusted to lower member stress and improve the feasibility of the optimisation problem.

Once the stiffness profile is approximated, the optimisation problem finds the optimal dimensions of the flexural rods, and the location of angular slots on the NES disc such that the lowest possible member stresses are obtained, while spatial restrictions are respected and the operation is kept below local resonance conditions. The material of the rod is defined here, along with spatial constraints and a rod resonance constraint. The user needs all the parameters in the Tab. 1 for the stress optimisation.

4. Identification and validation

The NES-host system in Fig. 11a will be used to validate the NES performance. The host system and NES parameters are identified independently using the experiments explained below.

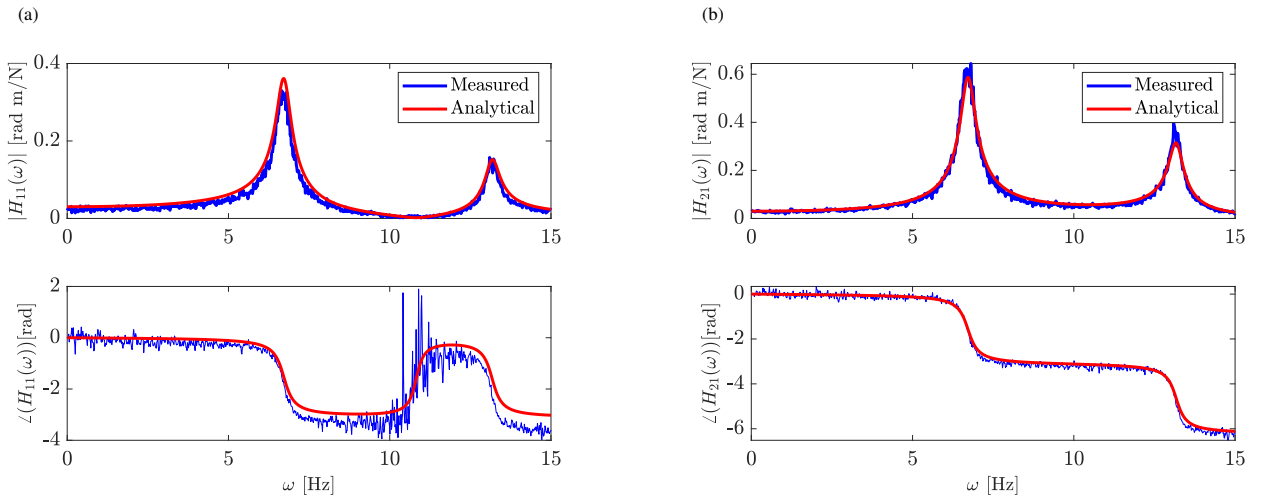


Figure 12: Measured and analytical Frequency Response Function (FRF)(s) of the host structure; (a) H_{11} and (b) H_{12} , where the upper plots show the magnitude and lower plots show the phase. The figures show good agreement between analytically predicted and measured FRFs.

4.1. Identification of host structure

The 2-DOF benchmark host system with NES is identified by applying a sine sweep excitation to the motor, which covers both eigenfrequencies of the structure. The angular displacement is measured at the inertias using encoders. Frequency Response Functions (FRFs), namely H_{11} and H_{21} , are obtained, where the indices i, j of $H_{i,j}$ indicate the response at inertia i due to a unit torque at inertia j . The measured FRFs are compared against analytically calculated values in Fig. 12. For the analytically calculated FRF, design values of the benchmark host are used to obtain the mass and stiffness matrix. The damping matrix is found through an insightful guess, where a diagonal damping matrix is assumed because the major contribution to damping comes from the bearings at the encoder. It is then fitted for the best result based on the root-mean-square error. This assumption is validated as seen in Fig. 12. The identified mass, stiffness and damping matrices are shown in Eq. (31). More details regarding the identification of the torsional

vibration benchmark system can be found in [90].

$$\mathbf{I} = \begin{bmatrix} 0.0125 & 0 \\ 0 & 0.0037 \end{bmatrix} \text{kg.m}^2, \quad \mathbf{C} = \begin{bmatrix} 0.0163 & 0 \\ 0 & 0.0032 \end{bmatrix} \frac{\text{Ns}}{\text{rad}}, \quad \mathbf{K} = \begin{bmatrix} 50.14 & -17.11 \\ -17.11 & 17.11 \end{bmatrix} \frac{\text{N}}{\text{rad}} \quad (31)$$

4.2. Identification of NES parameters

To identify the manufactured NES, both static and dynamic identification tests are performed. For both tests, only the inertia I_2 of the host system is attached, with the scheme and picture on Fig. 13, where the torsional stiffness is a combination of k_1 and k_2 . The dimensionless parameters of the identified NES-host is listed in Tab. 5.

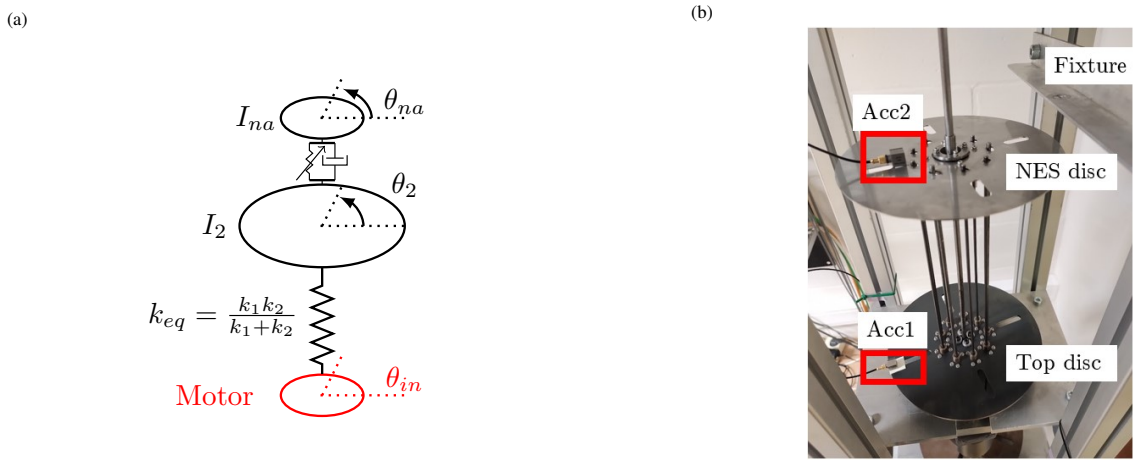


Figure 13: The experimental setup for identification of Nonlinear Energy Sink (NES). (a) The dynamical model of the modified setup for identification, where only the NES and its attached host inertia are connected to the motor. (b) The experimental setup with accelerometers attached to inertia I_2 (Top Disc) and NES inertia I_{na} . The fixture can be used to fix the NES inertia to the ground for the static test.

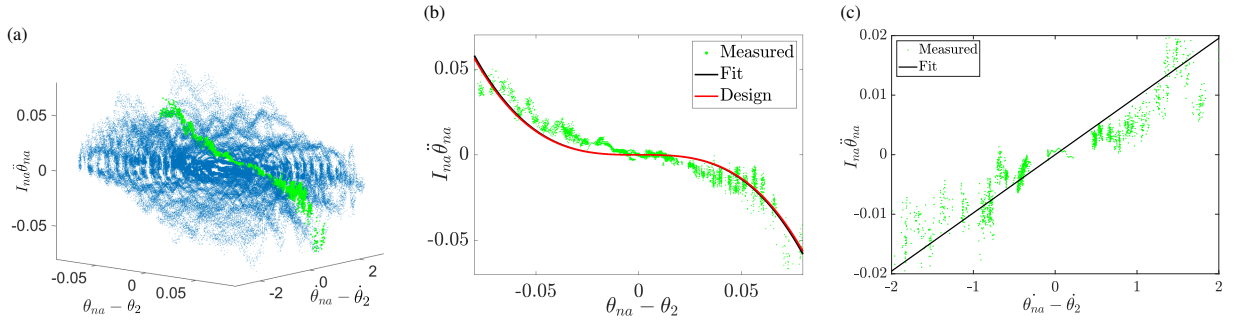


Figure 14: Results of the dynamic test for identification of the Nonlinear Energy Sink (NES). (a) The experimental Restoring Force Surface (RFS), where the blue points indicate all discrete measurements, and a slice of RFS where $\dot{\theta}_{na} - \dot{\theta}_2 \approx 0$ is indicated in green dots, where the damping force can be neglected. (b) The selected slice of points is fitted to a curve representing the nonlinear stiffness from measurements and compared to the designed nonlinear stiffness function. (c) a slice where $\theta_{na} - \theta_2 \approx 0$ to fit a viscous damping coefficient.

4.2.1. Dynamic test

For the dynamic test, the restoring force surface method is used [35, 91, 92, 93]. By measuring the acceleration between 2 degrees of freedom of a mechanical system, the nonlinear stiffness between these DOFs can be determined

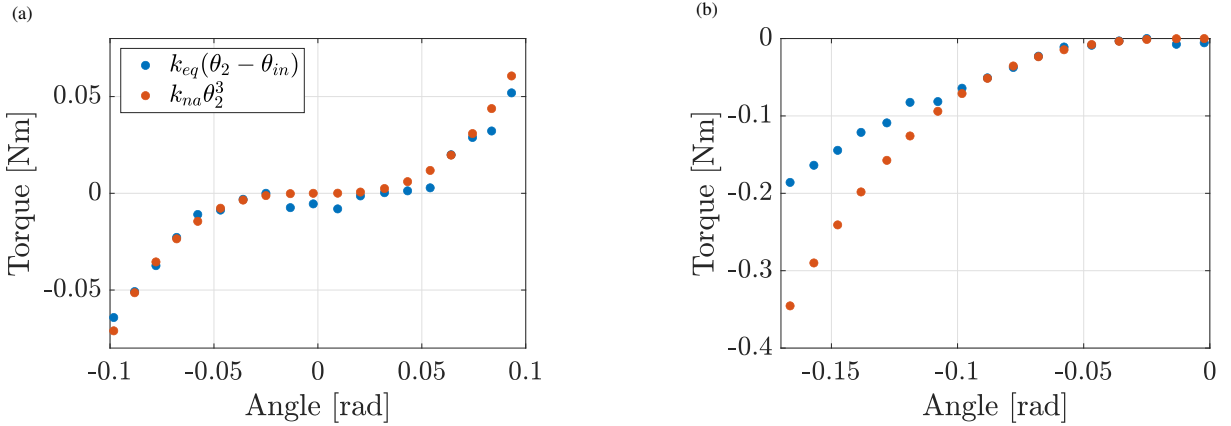


Figure 15: Results of the static test. (a) Comparison of the experimental nonlinear stiffness force (blue points) compared to the designed nonlinear stiffness force (orange points) shows good agreement within the maximum range of displacement, and (b) a lack of agreement outside the maximum range.

from a restoring force surface. Accelerometers are attached on the host system disc and NES disc as shown on Fig. 13b, and a sweep excitation is applied. The dynamical equation in Eq. (32) constitutes a surface in $\theta_{na} - \theta_2$ and $\dot{\theta}_{na} - \dot{\theta}_2$ space, with $I_{na}\ddot{\theta}_{na}$ determining the height. Slices of this surface where $\dot{\theta}_{na} - \dot{\theta}_2 \approx 0$ is used to fit the stiffness, while slices where $\theta_{na} - \theta_2 \approx 0$ are used to fit the viscous damping. The Figures 14b and 14c show a good fit between the designed and measured nonlinear stiffness ($k_{na} = 110 \text{ Nm}^{-3}$) and reveal the damping coefficient ($c_{na} = 0.0085 \text{ Ns.m}^{-1}$).

$$I_{na}\ddot{\theta}_{na} = -c_{na}(\dot{\theta}_{na} - \dot{\theta}_2) - k_{na}(\theta_{na} - \theta_2)^3 \quad (32)$$

4.2.2. Static test

In the static test, the NES inertia is fixed to the fixture (see Fig. 13b), such that the nonlinear stiffness is now connected to the ground. The angular displacement applied by the motor will result in the following static equilibrium between the nonlinear stiffness, the host system's stiffness, and the applied displacement of the motor:

$$k_{na}\theta_2^3 = k_{eq}(\theta_{in} - \theta_2) \quad (33)$$

The left and right side of Eq. (33) are plotted in Fig. 15 using the measurement from the encoders for θ_{in} and θ_2 and assuming the coefficients $k_{eq} = \frac{k_1 k_2}{k_1 + k_2}$ and $k_{na} = 110 \text{ Nm rad}^{-3}$. These show a good correspondence for the designed range ($\pm 0.1 \text{ rad}$) as shown in Fig. 15a. Near zero displacement, the computed torque has some mismatch, attributed to friction. For large angles outside the designed range, the stiffness no longer increases, as all rods are engaged, resulting in the linear characteristic (blue) in Fig. 15b, which does not follow the nonlinear function predicted by the orange curve.

ε	ξ	γ	$\omega_1 \text{ [rad/s]}$	ξ_{na}
0.088	0.296	82.68	42.4	0.269

Table 5: Parameters of the NES and the identified host system

4.3. Validity of the assumptions in CxA

The calculations presented in Section 2 used two main assumptions: (1) the assumption of the cubic nonlinear stiffness, compared to the piecewise-linear stiffness in the optimised design, and (2) the first-order CxA assumption, where the response is assumed to oscillate with a single frequency. The validity of these assumptions are treated in Appendix E and Appendix F respectively.

For the comparison of stiffness, the resonance frequency of an NES for both cases are compared across a range of response amplitudes. The analysis presented in Appendix E, concludes that the piecewise-linear stiffness performs effectively similar to the cubic stiffness within the design limit of amplitude (0.1 rad), and is also feasible 20% above this limit. For treating the validity of the first-order CxA, Appendix F presents a computation of the FR with the Harmonic Balancing (HB) method, computed for 50 harmonics. The results indicate that the first-order CxA is sufficient for the analysis, and the biggest difference occurs for high forcing, where the IRC fully merges into the FR curve.

4.4. Numerical validation

In this section, the NES-host system is numerically simulated for different forcing levels, to validate the analytical formulation for both low and high forcing, and to detect the merging of the IRC and the presence of SMR regime in the vicinity of resonance. Additionally, both cubic stiffness nonlinearity and its approximated piecewise-linear equivalent are compared; the identified parameter values in the above sections are used here. To this effect, a stepped-sine signal is the forcing signal, with frequency varying from 5 Hz to 8 Hz (which covers the resonance at 6.75 Hz), and 100 steps in between. The 'Runge-Kutta' (RK) algorithm of the command *ode45* is used in MATLAB for this simulation. The associated results and their discussion are presented next.

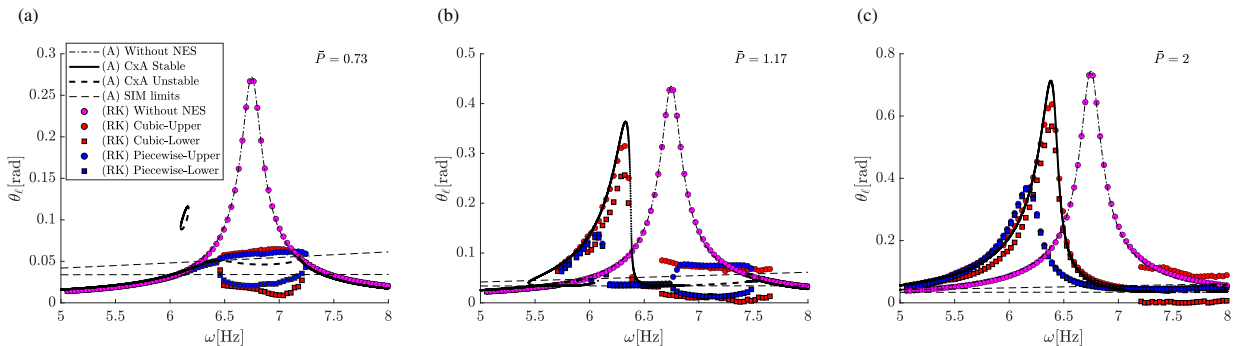


Figure 16: Frequency response of the host system from the analytical CxA and the numerical RK simulation, compared for both cubic and piecewise-stiffening NES. The legend indices (A) are from CxA, and (RK) are numerically simulated. The FRs are plotted for the forcing amplitudes: (a) $\bar{P} = 0.73$, (b) $\bar{P} = 1.17$, and (c) $\bar{P} = 2$.

Figure 16 shows the comparison of the analytical and numerical methods. The results are shown for three forcing levels, a forcing below the threshold for IRC merging ($\bar{P} = 0.73$ in Fig. 16a), a forcing with the merged IRC ($\bar{P} = 1.17$ in Fig. 16b), and a significantly high forcing ($\bar{P} = 2$ in Fig. 16c). The analytical results show the response of the unattenuated and attenuated host, with stable and unstable fixed points, and SIM limits obtained from CxA. The numerical RK simulation shows the response for the unattenuated host (without NES), and in the case of SMR, evaluates the maximum and minimum response levels from the envelope of the simulated oscillation (Fig. 2b shows such an envelope where the maximum and minimum can be obtained); the legends are titled Upper and Lower respectively. In the event that they coincide, the SMR is absent.

First, it is observed that the analytical results for the unattenuated host match perfectly with the RK simulation results for all three forcing levels. At low forcing as in Fig. 16a, it is seen that the analytically-predicted NS bifurcation is accurately tracked by the RK simulation, for both cubic and piecewise-linear stiffness, with minimal differences in the SIM limits. When the forcing is increased such that the IRC merges, then Fig. 16b shows deviations from CxA on the merged branch. Here, the host response with the cubic stiffness NES follows the merged branch and approximates its rise and fall frequency accurately, along with its peak magnitude. This is expected as the CxA calculations follow from the assumption of the cubic stiffness. It is noteworthy that a quasi-periodic response is observed in a narrow frequency band around the merged IRC peak, where a loss of linear stability is not predicted by CxA. The response with the piecewise-linear NES also jumps to the merged IRC but exits the branch at a comparatively lower frequency, therefore not achieving the higher CxA-predicted peak magnitude. This is because the piecewise-linear stiffness is not designed for response $\theta_{na} - \theta_\ell > 0.1$ rad, as is the case here, and no longer approximates well the corresponding cubic nonlinearity (refer Appendix E) Furthermore, the NS-bifurcation at 6.7 Hz and 7.8 Hz is also predicted well by the RK simulation, for both stiffness cases. In the case of high forcing, Fig. 16c shows that the host-cubic NES response for both RK and CxA correlate well, while deviations, especially in the peak response, are observed from the host-piecewise NES response. The discussion above concludes that the first-order CxA approximates well the host response with the cubic stiffness NES, while for the case with the piecewise-linear NES the correlation with the cubic stiffness only extends till its maximum design angle. Furthermore, the piecewise-linear NES peak amplitude is much lower in the case of the IRC merging. Thus, this design is safer than the cubic NES if it is excited beyond its intended limit.

4.5. Experimental validation of the first mode mitigation

In this section, the primary objective of the design is considered, i.e. the attenuation of the first natural frequency of the host. In this regard, FR prediction from CxA (Eqs. (16) and (17)) is compared to experimental results to explore the general agreement between the results obtained and also to validate the choice of the nonlinearity and its parameter values. The parameter values from the identification of the NES and of the host system are given in Tab. 5.

A sine sweep signal from 5.5 Hz to 8.5 Hz frequency and of amplitude ($|\theta_{in}|$) of 0.005, 0.006 or 0.008 rad is provided by the motor to I_1 of the host system (refer to Fig. 11a). The angle measurements are acquired by belt-driven encoders attached to each of the respective inertias. The measurement data is then filtered, and the envelope of oscillation is extracted. At each time instant, corresponding to a certain frequency of the applied sweep, the response magnitude is obtained; thereby, an experimental frequency response is obtained. The experiments are done with and without the NES attached. Figure 17 shows the encoder measurements at inertia I_2 of the host system with the NES attached. Here, the measurement shows the expected Neimark-Sacker bifurcation in the vicinity of the 1:1 resonance ($\omega_1 = 6.75$ Hz), where the quasi-periodic SMR behaviour is observed.

The analytical FR and the experimental FR are superimposed in Fig. 18 where legends (A) stand for analytical and (E) for numerical results. A clear agreement can be seen between the experimental and analytical results, thus validating the CxA method and its assumptions. Near the resonance, it can be seen that the experimental FR with NES is restricted by the dashed lines from the SIM, experimentally confirming that SMR is restricted by the SIM minima and maxima. It can be inferred that for all three excitation cases, there has been a significant reduction and saturation of the resonant response, but with a major caveat: the presence and attachment of an Isolated Resonance Curve (IRC) at higher forcing levels.

For the input excitation of $|\theta_{in}| = 0.005$ rad (Fig. 18a), the resonant response (at $\omega_1 = 6.75$ Hz) of the host with the NES is reduced by $\sim 82\%$ compared to the unattenuated case. Complexification-Averaging predicts a region of

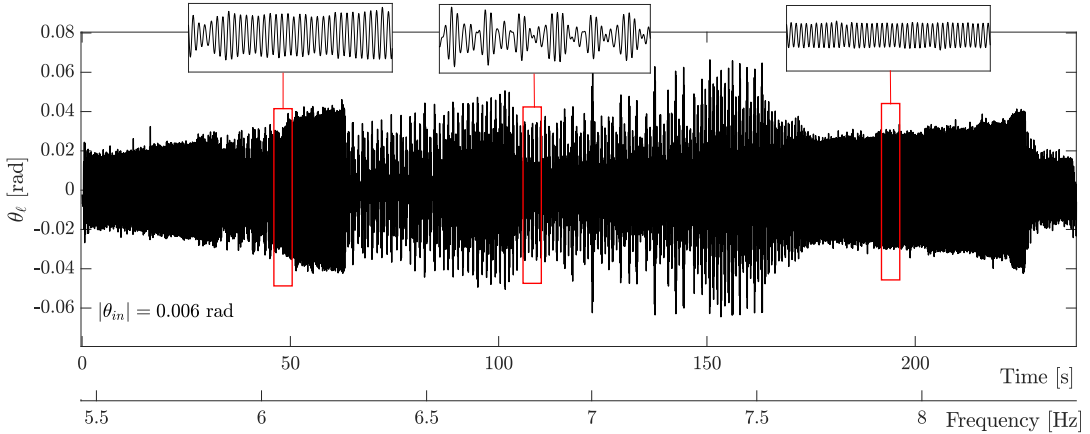


Figure 17: Measurement of the host system with the Nonlinear Energy Sink (NES) attached. A sine sweep excitation with frequency varying from 5.5 Hz to 8.5 Hz and amplitude $|\theta_{in}| = 0.006$ rad is provided by the motor, and the angle encoder measurement of the inertia I_2 attached to the NES is shown here (refer Fig. 11a). Zoomed-in views of the measured responses are shown for the same time interval.

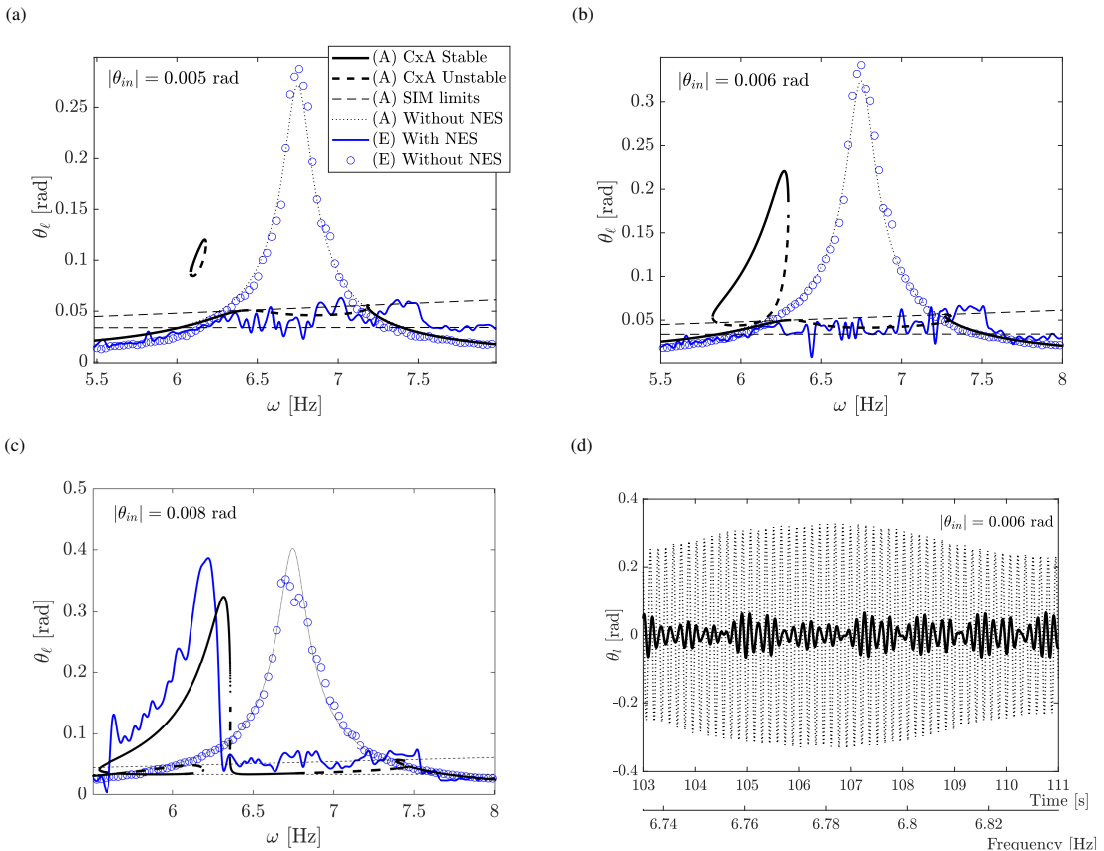


Figure 18: Frequency response of the host system for various input excitations; (a) $|\theta_{in}| = 0.005$ rad (b) 0.006 rad (c) and 0.008 rad. The legends (A) indicate the response envelope obtained from Complexification-Averaging with its stable and unstable fixed-points, also with the limits of the Strongly Modulated Response (SMR) around 1:1 resonance indicated. The experimental response envelope is indicated by legends (E). (d) The time response of the host system with (—) and without NES (.....) for $|\theta_{in}| = 0.006$ rad, showing the SMR response around resonance.

linear instability at resonance; this is attributed to the inception of the quasi-periodic SMR regime, with its modulating envelope as seen in Fig. 2b, which is also seen in the experiment (refer Fig. 17 for $|\theta_{in}| = 0.006$ rad, where the middle panel of the zoomed-in response shows the response modulation). In a narrow frequency band from 6.1 Hz to 6.2 Hz an IRC is formed in the analytical FR, undetected by the experiment as it is not connected to the main curve.

At $|\theta_{in}| = 0.006$ rad (see Fig. 18b), the resonant response is diminished as before ($\approx 84\%$ reduction), however, the IRC expands to almost merging with the main resonance curve. The response after attachment of the IRC is observed in Fig. 18c for $|\theta_{in}| = 0.008$ rad with a large amplitude response predicted by the measurement. Still, this response is lower than the resonant response of the unattenuated host system. Also, the saturated resonant response shows $\sim 87\%$ vibration suppression. The rise and fall frequency and the response magnitude on the attached curve are also predicted reasonably well by the CxA method. Minor deviations can be attributed to the lack of higher-order terms in the ansatz of the proposed CxA solution, as is recommended for the response on the merged IRC at high forcing amplitudes (refer Appendix F). This lack of correlation could also be due to the deviation of the actual, piecewise-linear stiffness from cubic nonlinear stiffness at high amplitudes (refer Appendix E), as the NES response on the merged IRC is above its design limit. A comparison of the host system's response measured with and without the NES is shown in Fig. 18d, for a sweep through the resonant frequency. Here, a clear reduction in the response is observed after the attachment, in addition to the SMR behaviour predicted by the SIM.

5. Mitigation performance on the second mode

The analysis and tuning of the NES elaborated in the previous sections is to tune the NES to absorb the first resonance of the host. However, the performance of the NES can also be explored in relation to the second resonance of the host, with a focus on the broadband attenuation capability of the NES. For analytical computations, Sections 2.1 and 2.2 can be referred to, where the computations are performed for the EOM reduced on the second mode. The host system has been re-identified as per Sec. 4.1 to have the following system matrices, as the tests on the second mode were conducted at a later period in time. The dimensionless parameters are also given in Tables 6 and 7 respectively.

$$\mathbf{I} = \begin{bmatrix} 0.0125 & 0 \\ 0 & 0.0037 \end{bmatrix} \text{kg.m}^2, \quad \mathbf{C} = \begin{bmatrix} 0.0319 & 0 \\ 0 & 0.0063 \end{bmatrix} \frac{\text{Ns}}{\text{rad}}, \quad \mathbf{K} = \begin{bmatrix} 49.6235 & -16.5978 \\ -16.5978 & 16.5978 \end{bmatrix} \frac{\text{N}}{\text{rad}} \quad (34)$$

ε	ξ	γ	ω_1 [rad/s]	ξ_{na}
0.090	0.579	83.809	42.115	0.273

Table 6: Re-identified parameters pertaining to the first mode of the host

ε	ξ	γ	ω_2 [rad/s]	ξ_{na}
0.111	0.231	22.24	81.744	0.141

Table 7: Re-identified parameters pertaining to the second mode of the host

The analysis of the FR is repeated here as shown in Fig. 19. Note that since dimensionless forcing \bar{P} varies between the modes (as it depends on ω_i), and the dimensional force F_1 is given alongside for a meaningful comparison. From Fig. 19a for the host response at the first resonance, we see that as the forcing level increases, a NS bifurcation occurs

in the vicinity of the 1:1 resonance, resulting in an SMR regime ($\bar{P} = 0.72$). As the forcing increases, the presence of an IRC is noticed, which merges to the main FR branch at $\bar{P} = 0.99$, and enlarges further as seen for $\bar{P} = 1.27$. To compare, Fig. 19b shows the host FR in the vicinity of the second mode; at $F_1 = 0.3N$ both the SMR regime and IRC are absent unlike what's seen for the first mode. Similar trends in the bifurcations, as in Fig. 19a, is observed but at a much higher forcing. As such, the NES is also able to tackle the second mode, but for higher forcing amplitudes.

For the second mode, the IRC inception is observed at $\bar{P} = 0.41$ and its merging is observed around $\bar{P} = 0.6$. Regarding resonant attenuation, at $\omega = 6.7$ Hz, a reduction of 61%, 72% and 78% for $\bar{P} = 0.72, 0.99$ and 1.27 respectively. Similarly, we observe a reduction of 43%, 65.5%, 75% and 82.5% for $\bar{P} = 0.14, 0.30, 0.41$ and 0.60 respectively, showing that the NES can still effectively function at the second mode. Note that $\bar{P} = 0.14$ has the lowest reduction due to the response not triggering an SMR regime (absence of NS bifurcation). The comparison of the IRC tracking for both modes are treated in Fig. 19c where it is observed that forcing thresholds (dimensional) for appearance and merging are higher for the second mode when compared to the first.

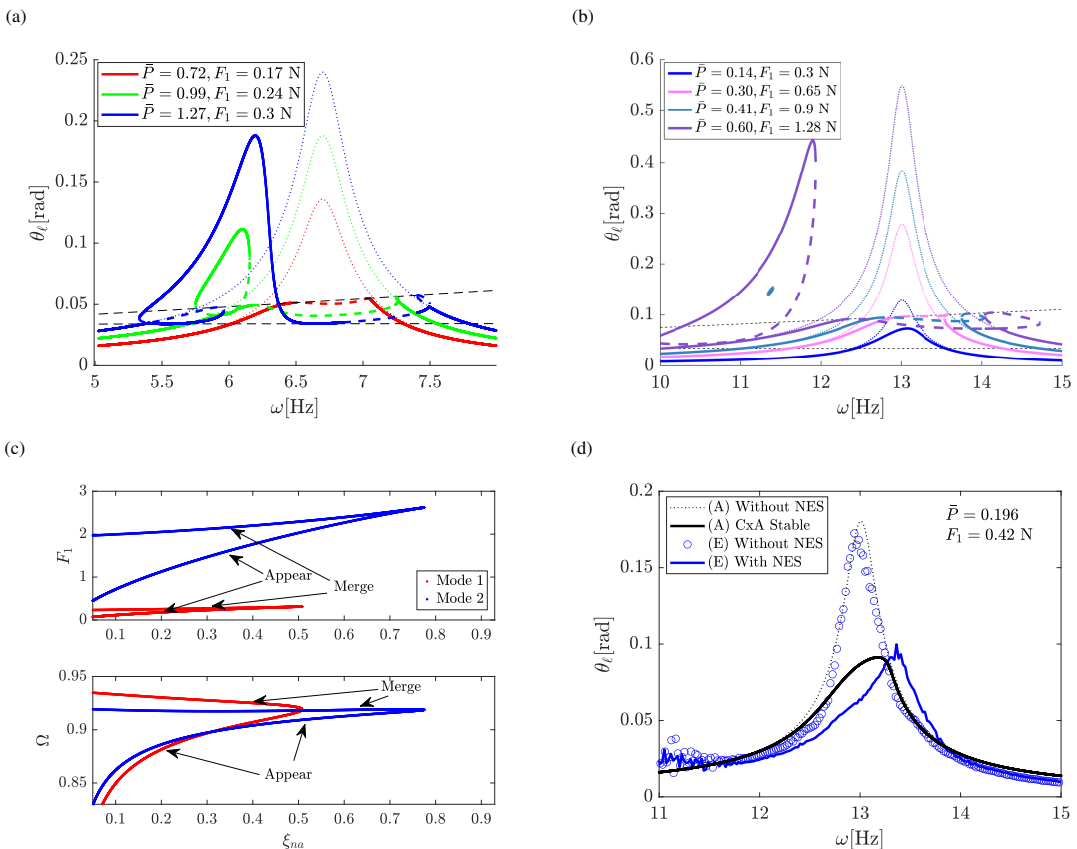


Figure 19: The Frequency Response (FR) analysis for the second mode of the host. The FR of the attenuated (NES attached) host system (a) in the vicinity of the first host resonance, for three different forcing levels, and (b) in the vicinity of the second host resonance, for four different forcing levels. All solutions with NES attached (stable —) and unstable (---) solutions, and without NES attached (...) are indicated. (c) The tracking of the Isolated Resonance Curve (IRC) in the vicinity of the first and second resonance, showing parameter combinations for IRC appearing and merging onto the main FR branch. (d) Analytical FR compared to experimental FR; legends (A) and (E) indicate analytical and experimental results, respectively. All system parameters for the simulations in (a)-(d) are from Tabs. 6 and 7.

An experimental validation at the second mode is also provided in Fig. 19d, where the experiment and analysis match perfectly for the unattenuated host, and for the attenuated case, slight deviations from the CxA results are

observed, possibly due to the errors in the sine sweep excitation. Higher forcing levels were not possible on the experimental setup, but this level still shows a significant reduction compared to no absorber.

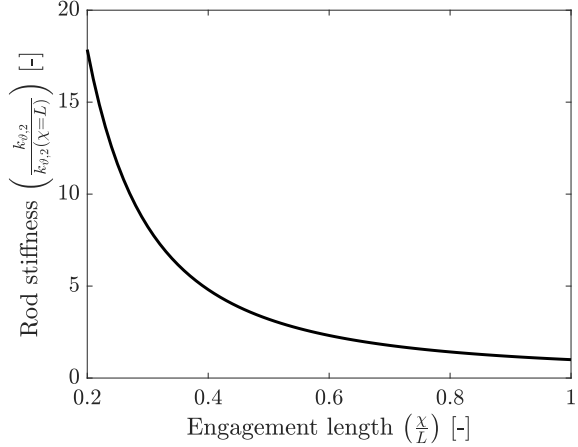


Figure 20: The variation in the bending stiffness $k_{\theta,2}$ of flexural rod ($h = 2$), on changing the engagement length χ relative to the length L of the rod. The stiffness is scaled to the value at $\chi = L$. All other parameters correspond to the optimised NES design for rod ($h = 2$) in Tab. 2.

NES modifications for better multi-modal attenuation

From a practical viewpoint, it could be argued that the NES lacks effectiveness if the host system is unable to generate the forcing level required for an NS bifurcation ($a > \sqrt{Z_a^+}$ in Fig. 2a). This however can be solved in the design presented in Fig. 7b where the rotary bearing assembly could be moved, modifying χ in Eq. (20), which in-turn affects the scaling of the dimensionless force \bar{P} by changing γ (see Eq. (9)). The variation in rod stiffness for a change in γ , for all other parameters constant, is shown in Fig. 20 below. Here the design stiffness at $\chi = L$ is compared to its value as χ changes. When χ is lowered, the stiffness of the rod increases, with a more rapid increase at low values ($\frac{\chi}{L} < 0.4$). This increases k_{na} and γ in a proportional manner, with the dimensionless force $\bar{P} \propto \sqrt{\gamma}$, allowing the NES to reach conditions triggering NS bifurcation if the host forcing levels are too low. A caveat, however, is that the first mode has a potential for an IRC to initiate and merge at high forcing, although the IRC upper branch has lower response than an unattenuated host at resonance. Therefore, a hybrid design could be explored where χ can be modified during its operation, and changes between resonances, to obtain optimal operational conditions for the NES.

6. Conclusions

The analysis and design of a piecewise-linear stiffness Nonlinear Energy Sink (NES) for attenuating resonant vibrations in a torsional setup has been successfully explored. For the analysis, a n -DOF host system with a NES attached at a single location is considered. The corresponding EOM is reduced to a single mode of the host system, to be mitigated by the NES in 1:1 resonance regime. Afterwards, the envelope of oscillation is analysed with the Complexification-Averaging (CxA) method, from which the equations for the Slow Flow Dynamics, and its invariant manifolds are obtained. The explained design methodology is a complete toolchain that assists in NES implementation by proposing a theoretical framework to obtain an optimal nonlinear stiffness parameter, for the attenuation of a single mode. It then relates this to aspects of structural integrity and practical dimensional restrictions, applicable to a wide range of systems. An intuitive perspective of the following design optimisation is also provided to further understand

the influences of design parameters. Experimental FRs in the vicinity of the first mode (chosen for mitigation) of the host are presented, along with showcasing the NES performance for the second mode, presenting adaptations for better performance in either case. The study reveals the following key insights and showcases results from its design methodology:

- The CxA method has been validated using experiments on different levels of forcing, for a strong nonlinearity, on both of the host system modes. This supports the argument of using CxA, even in its first-order approximation.
- The CxA method predicts correctly the presence of the SMR regime in the vicinity of 1:1 resonance and its response limits are also calculated. It could also be used to detect the presence of an Isolated Resonance Curve (IRC) in the frequency response, undetected by the experimental tests.
- The parametric analysis of the SIMs reveals that a lower NES damping ξ_{na} and higher dimensionless forcing \bar{P} favour the inception of a NS bifurcation in the FR, however, these changes also increase the potential for the inception of a sub-resonant IRC.
- The inception of the IRC occurs at a threshold value of host forcing, for a given NES damping. Decreasing the NES stiffness parameter γ , and increasing NES damping ξ_{na} raises the forcing threshold, as seen from the FR analysis and from IRC tracking using the Singularity method. The latter method reveals a threshold on damping above which IRCs are absent. However, increasing NES damping reduces the frequency band of SMR response and also increases the response at resonance. At forcing levels higher than the threshold for IRC inception, the IRC enlarges and merges to the main resonance curve. This has been identified by both the experiment and CxA response envelopes.
- The implemented NES prototype offers a significant attenuation of the resonant response at the first mode; 80% - 87% attenuation for a broad range of input excitation ($F_1 = |\theta_{in}|k_1 = 0.17N$ to $0.23N$) and 61%-78% attenuation for $F_1 = 0.17N$ to $0.3N$ in the case of the re-identified host model. But its performance is limited at high forcing by the presence and enlargement of an IRC at a sub-resonant frequency band. However, even in this case, the response amplitude is less than that of the unattenuated host system resonant response.
- The evaluation of the NES for the second mode also shows good attenuation, 43% to 83% response reduction for $F_1 = 0.3N$ to $1.28N$, where better attenuation is observed at forcing levels where NS bifurcations occur. Also, the forcing levels triggering the bifurcation, as well as IRCs for the second mode are much higher compared to that for the first mode.
- The physical restriction on the forcing level can be overcome by increasing the stiffness parameter γ via lowering the engagement length χ , where the rods engage with the NES inertia; this increases dimensionless forcing \bar{P} and allows an optimal response for the second mode. However, this makes the first mode response sub-optimal with the merging of an IRC. A potential solution is to have a design that adjusts χ according to the mode to be mitigated.

For tuning the NES, a SIM-based tuning methodology based on a first-order CxA has been implemented in this paper. A modal reduction of the host dynamics around a single mode is performed. While this allows for simple analytical formulations that enable fast tuning, there are some notable drawbacks in specific situations. The single-mode assumption is insufficient to account for cases when the excitation is distant from the chosen 1:1 resonance,

in such cases a multi-modal approach is preferred. Then, the SIM-based tuning for a single mode can be appended to include the interactions of other modes. The research presented by the co-author Kevin et al. [51] can serve as a starting point. For the case when the excitation is multi-harmonic, the CxA then needs to also incorporate these harmonics in its envelope variable formulation. Another reason to include higher harmonics is at high forcing levels, often leading to responses with a fully-merged IRC (Appendix F).

The design and analysis presented in this research has the host system under harmonic excitation, and the response behaviour under transient and random excitation is noticeably different. Under transient loading, the SMR behaviour is not observed as the damping in the system prevents a sustained oscillation, instead the TET phenomenon occurs where the energy from the excitation is localised irreversibly in the NES to be damped out, provided the excitation threshold to initiate TET is overcome [23]. The analysis of the SIM in section 2.4.1 can be referred, where the initial condition $a(t = 0) \geq \sqrt{Z_a^+}$ triggers TET.

Under stochastic loading, the system behaviour is altered at each cycle and the deterministically evaluated SIM predicts well the slow oscillations of the envelope, however, the fold points (SIM maxima and minima) are not representative of the fast-dynamics [94]. A scope of future research is to consider numerical Monty Carlo methods [94] or the theoretical study of noisy slow-flow systems [95] for better analysis of such systems. Nonetheless, the NES design toolchain presented here can be easily adapted to changing theoretical analysis, and changing requirements and supports a direct implementation on a torsional host system.

Appendix A. Stability of SIM

The stability of the solutions on the SIM is computed with the 2nd equation of Eq. (14), rewritten below:

$$B' = -\frac{1}{j2\sqrt{X}} (j2\sqrt{X}A' - XB - XA + j\xi_{na}\sqrt{X}B + 3B|B|^2) \quad (\text{A.1})$$

This equation is linearised around the fixed points A_{eq} and B_{eq} . The fixed point for the magnitude is found from the solutions of Eq. (16), and for the phase from Eq. (15) by substituting $B_{eq} = \frac{b}{2}e^{j\beta}$ and $A_{eq} = \frac{a}{2}e^{j\alpha}$. Thus, the linearisation proceeds as:

$$\begin{aligned} B &= B_{eq} + \Delta B \\ B' &= \Delta B' \end{aligned} \quad (\text{A.2})$$

Which is expanded as:

$$\Delta B' = \left. \frac{\partial B'}{\partial B} \right|_{B=B_{eq}} \Delta B + \left. \frac{\partial B'}{\partial B^*} \right|_{B=B_{eq}} \Delta B^* \quad (\text{A.3})$$

$$\Rightarrow \begin{bmatrix} \Delta B' \\ (\Delta B')^* \end{bmatrix} = \underbrace{\begin{bmatrix} a_{11} & a_{12} \\ a_{21} & a_{22} \end{bmatrix}}_{\Sigma} \begin{bmatrix} \Delta B \\ \Delta B^* \end{bmatrix} \quad (\text{A.4})$$

where the matrix coefficients are:

$$\begin{aligned} a_{11} = a_{22}^* &= \frac{1}{2\sqrt{X}} (-jX - \xi_{na}\sqrt{X} + j6BB^*|_{B=B_{eq}}) \\ a_{12} = a_{21}^* &= \frac{1}{2\sqrt{X}} (j3B^2|_{B=B_{eq}}) \end{aligned} \quad (\text{A.5})$$

Finally, the stability is determined by computing the eigenvalues of Σ matrix in equation (A.4). If any eigenvalue has a positive real part, the solution is unstable.

Appendix B. Stability of slow flow dynamics

The stability of the asymptotic solution of Eq. (14) is computed from the linear stability around fixed points of A and B , called A_{eq} and B_{eq} respectively. Equation (14) can be rewritten as:

$$\begin{aligned} A' &= \frac{1}{2j\sqrt{X}} \left(\frac{\varepsilon\bar{P}}{2} - j\varepsilon\xi\sqrt{X}A - \varepsilon\sigma A - \varepsilon(-j\xi_{\text{na}}\sqrt{X}B - 3B^2B^*) \right) \\ B' &= \frac{1+\varepsilon}{2j\sqrt{X}} \left(XB + XA - j\xi_{\text{na}}\sqrt{X}B - 3B^2B^* - \frac{1}{1+\varepsilon} \left(\frac{\varepsilon\bar{P}}{2} - j\varepsilon\xi\sqrt{X}A - \varepsilon\sigma A + \varepsilon(XB + XA) \right) \right) \end{aligned} \quad (\text{B.1})$$

The fixed point for the magnitude is found from the solutions of Eqs. (16) and (17), and the fixed points for the phase from Eq. (15) by substituting $B_{\text{eq}} = \frac{b}{2}e^{j\beta}$ and $A_{\text{eq}} = \frac{a}{2}e^{ja}$. Thus, the linearisation proceeds as:

$$\begin{aligned} B &= B_{\text{eq}} + \Delta B \\ B' &= \Delta B' \\ A &= A_{\text{eq}} + \Delta A \\ A' &= \Delta A' \end{aligned} \quad (\text{B.2})$$

Which is expanded as:

$$\begin{aligned} \Delta A' &= \frac{\partial A'}{\partial A} \Big|_{\text{eq}} \Delta A + \frac{\partial A'}{\partial A^*} \Big|_{\text{eq}} \Delta A^* + \frac{\partial A'}{\partial B} \Big|_{\text{eq}} \Delta B + \frac{\partial A'}{\partial B^*} \Big|_{\text{eq}} \Delta B^* \\ \Delta B' &= \frac{\partial B'}{\partial A} \Big|_{\text{eq}} \Delta A + \frac{\partial B'}{\partial A^*} \Big|_{\text{eq}} \Delta A^* + \frac{\partial B'}{\partial B} \Big|_{\text{eq}} \Delta B + \frac{\partial B'}{\partial B^*} \Big|_{\text{eq}} \Delta B^* \end{aligned} \quad (\text{B.3})$$

$$\implies 2j\sqrt{X} \begin{bmatrix} \Delta A' \\ (\Delta A')^* \\ \Delta B' \\ (\Delta B')^* \end{bmatrix} = \underbrace{\begin{bmatrix} a_{11} & a_{12} & a_{13} & a_{14} \\ a_{21} & a_{22} & a_{23} & a_{24} \\ a_{31} & a_{32} & a_{33} & a_{34} \\ a_{41} & a_{42} & a_{43} & a_{44} \end{bmatrix}}_{\Sigma} \begin{bmatrix} \Delta A \\ \Delta A^* \\ \Delta B \\ \Delta B^* \end{bmatrix} \quad (\text{B.4})$$

The matrix elements are described below:

$$\begin{aligned} a_{12} &= a_{21} = a_{32} = a_{41} = 0 \\ a_{11} &= -a_{22}^* = -\varepsilon\sigma - j\varepsilon\xi\sqrt{X} \\ a_{13} &= -a_{24}^* = j\varepsilon\xi_{\text{na}}\sqrt{X} + 6\varepsilon BB^*|_{B=B_{\text{eq}}} \\ a_{14} &= -a_{23}^* = 3\varepsilon B^2|_{B=B_{\text{eq}}} \\ a_{31} &= -a_{42}^* = \varepsilon\sigma + j\varepsilon\xi\sqrt{X} + X \\ a_{33} &= -a_{44}^* = X - \frac{1+\varepsilon}{\varepsilon}a_{13} \\ a_{34} &= -a_{43}^* = -\frac{1+\varepsilon}{\varepsilon}a_{14} \end{aligned} \quad (\text{B.5})$$

The stability is then determined from the eigenvalues of $\frac{\Sigma}{2j\sqrt{X}}$. The presence of eigenvalues with positive real part implies unstable solution.

Appendix C. Existence of SIM fold points

The possibility of the SMR regime is dependent on the presence of fold bifurcations on the SIM. The SIM extrema are the roots of the equation obtained by differentiating Eq. (16) w.r.t Z_b , as shown below:

$$\frac{\partial Z_a}{\partial Z_b} = Z_b^2 - \frac{16}{9}XZ_b + \frac{16}{27}(X\xi_{na}^2 + X^2) = 0 \quad (C.1)$$

Equation (C.1) given above is quadratic and has two roots, where they have to be positive and real to ensure that the two fold bifurcation points exist (i.e. the maxima and minima of SIM in Fig. 2). Therefore, when the determinant of Eq. (C.1) is positive, real roots are guaranteed. Hence, we have the condition:

$$\begin{aligned} \frac{16}{9}X^2 - \frac{4}{3}(X\xi_{na}^2 + X^2) &> 0 \\ \implies X &> 3\xi_{na}^2 \end{aligned} \quad (C.2)$$

Furthermore, to ensure that only positive roots are obtained, Eq. (C.1) is rewritten in terms of its roots $Z_{b,1}$ and $Z_{b,2}$, where the sum and product of the roots are written as:

$$\begin{aligned} Z_{b,1} + Z_{b,2} &= \frac{16}{9}X \\ Z_{b,1}Z_{b,2} &= \frac{16}{27}(X\xi_{na}^2 + X^2) \end{aligned} \quad (C.3)$$

If both the sum and product of the roots are positive, then the roots $Z_{b,1}$ and $Z_{b,2}$ are also positive. This is guaranteed from the right-hand side, as $X \in \mathbb{R}_+$ and $\xi_{na} \in \mathbb{R}_+$. Therefore, the only criterion to ensure the SIM bifurcation is Eq. (C.2). The bifurcation is visualised in simulations and measurements as an SMR regime if the response threshold of $(\sqrt{Z_b^-}, \sqrt{Z_a^+})$ is overcome by the forcing.

Appendix D. Sensitivity analysis

In this section, the sensitivity of the chosen design (refer Tab. 2) to deviations in the design parameters of the NES, namely, flexural rod diameter d_h , length L , engagement location the rod length χ and radial distance of engagement R_h are studied; the subscript h refers to those of the h^{th} stiffness increment. The sensitivity is analysed for the individual stiffness contributions $k_{\theta,h}$, and the maximum rod stress $\sigma_{max,h}$, based on Eqs. (20) and (25) respectively, where a Jacobian-based local sensitivity analysis is conducted. Tables D.8 and D.9 show the calculated sensitivity factors, and Eq.(D.1) shows the computation of the Jacobian for a given function.

$$\begin{aligned} \mathbf{J}_f &= \left[\frac{\partial f}{\partial d_h}, \frac{\partial f}{\partial L}, \frac{\partial f}{\partial \chi}, \frac{\partial f}{\partial R_h} \right] = [S_{d_h}, S_L, S_\chi, S_{R_h}] \\ \text{where } f &= k_{\theta,h}(d_h, L, \chi, R_h) \quad \text{or} \quad f = \sigma_{max,h}(d_h, L, \chi, R_h) \end{aligned} \quad (D.1)$$

Rod Index (h)	$S_{d_h} [N/m^2]$	$S_L [N/m^2]$	$S_\chi [N/m^2]$	$S_{R_h} [N/m^2]$
2	228.4	-2.2	-0.3	12.3
3	296.6	-3.0	-0.4	16.4
4	433.1	-5.0	-0.6	26.1

Table D.8: Sensitivity of the rod stiffness ($f = k_{\theta,h}(d_h, L, \chi, R_h)$) of the optimised NES to deviation in design parameters.

Rod Index (h)	$S_{d_h}(\times 10^9) [Pa/m]$	$S_L(\times 10^9) [Pa/m]$	$S_\chi(\times 10^9) [Pa/m]$	$S_{R_h}(\times 10^9) [Pa/m]$
2	-2.02	0.05	0.0	0.22
3	-1.86	0.05	0.0	0.21
4	-1.53	0.05	0.0	0.19

Table D.9: Sensitivity of the rod maximum bending stress ($f = \sigma_{max,h}(d_h, L, \chi, R_h)$) of the optimised NES to deviation in design parameters.

The rod stiffness sensitivity analysis in Tab. D.8 infers that the rod diameter d_h and the radial distance R_h from the center of rotation form the major parameters influencing the stiffness, where the former parameter is about 20 times more significant. This is also reasoned by inspecting the formula for stiffness in Eq. (20). The individual sensitivities of each piecewise-linear segment also increase progressively (per rod h). Therefore, there should be strict manufacturing controls on d_h , and R_h to a lesser extent, such that design objectives are met. Similarly, for the stress sensitivity analysis in Tab. D.9, d_h and R_h are more significant compared to other parameters, with the former more influential than the latter. Notably, the sensitivity to parameters decreases for higher stiffness increments (as h increases) and the first rod ($h = 2$) is the most critical. In this regard, the relative change in the sensitivity values is lesser than that for the stiffness sensitivity. Besides, deviations in the stiffness affect the function of the NES, while deviations in the stress are less significant since the optimisation results show the rod stresses to be significantly lower than the material endurance limit. To conclude, rod diameter d_h and radial location R_h require precision, with more importance given to the rods of the last stiffness increment.

Appendix E. Frequency-Energy Plot

Here, the Frequency-Energy relation of a cubic hardening and a piecewise stiffness are compared. An SDOF system with mass m_a with this stiffness is compared:

$$m_a \ddot{x}_a + f_{nl}(x_a) = 0. \quad (\text{E.1})$$

By then applying a standard harmonic balance technique [69] for frequency ω , Eq. (E.1) is transformed into:

$$\begin{aligned} & \frac{\omega}{2\pi} \int_0^{\frac{2\pi}{\omega}} -m_a A \omega^2 \sin^2(\omega T) dT \\ & + \frac{\omega}{2\pi} \int_0^{\frac{2\pi}{\omega}} f_{nl}(A \sin(\omega T)) \sin(\omega T) dT = 0 \Rightarrow \\ & m_a A \omega^2 \sin(\omega T) - \frac{\omega}{2\pi} \int_0^{\frac{2\pi}{\omega}} f_{nl}(A \sin(\omega T)) \sin(\omega T) dt = 0 \end{aligned} \quad (\text{E.2})$$

where the integral is the first harmonics from the truncated Fourier series. Two stiffness types are considered, which possess nonlinear restoring forces $f_{nl}(x_a)$ as depicted in Figure 8a. The relation between frequency and amplitude is

found by solving the integral in Eq. (E.2), which yields for the cubic stiffness:

$$f_{\text{nl}}(x_a) = k_{\text{na}} x_a^3 : \quad m_a \omega^2 = k_{\text{na}} \frac{3A^2}{4} \quad (\text{E.3})$$

For the piecewise stiffness, the relation depends on how many of the rods are engaged. For piecewise functions, the integral for HB needs to be solved in steps, where a full explanation is given in [55]. The case of 3 stiffness increments where the stiffness is zero for some vibration around 0 is studied. The piecewise stiffness implemented in this work:

- $x_1 < A < x_2$ where k_1 engages

$$m_a \omega^2 = \frac{k_1}{A\pi} \left(-2x_1 \sqrt{\frac{A^2 - x_1^2}{A^2}} + A \left(\pi - 2 \arcsin \left(\frac{x_1}{A} \right) \right) \right) \quad (\text{E.4})$$

- $x_2 < A < x_3$ where k_1 and k_2 engages

$$m_a \omega^2 = \frac{1}{A\pi} \left(k_1 \left[-2A \arcsin \left(\frac{x_1}{A} \right) - 2x_1 \sqrt{1 - \left(\frac{x_1}{A} \right)^2} + A\pi \right] + k_2 \left[-2A \arcsin \left(\frac{2x_1}{A} \right) - 4x_1 \sqrt{1 - \left(\frac{2x_1}{A} \right)^2} + A\pi \right] \right) \quad (\text{E.5})$$

- $A > x_3$ where k_1 , k_2 and k_3 engages

$$\begin{aligned} m_a \omega^2 = & \frac{1}{A\pi} \left(-2x_1 \left[3 \sqrt{1 - \left(\frac{3x_1}{A} \right)^2} k_3 + 2 \sqrt{1 - \left(\frac{2x_1}{A} \right)^2} k_2 + \sqrt{1 - \left(\frac{x_1}{A} \right)^2} k_1 \right] \right. \\ & \left. + A \left[\pi(k_1 + k_2 + k_3) - 2k_1 \arcsin \left(\frac{x_1}{A} \right) - 2k_2 \arcsin \left(\frac{2x_1}{A} \right) - 2k_3 \arcsin \left(\frac{3x_1}{A} \right) \right] \right) \end{aligned} \quad (\text{E.6})$$

For the design in this work, where $k_{\text{na}} = 110 \text{ N/m}^3$ and the piecewise-linear stiffness increments from Eqs. (21) and (23), the characteristic and corresponding frequency-amplitude relations are given in Fig. E.21. The piecewise-linear stiffness approximates the cubic characteristic within the designed limit of 0.1, Fig E.21a. The frequency-amplitude plot in Fig. E.21b shows a good correspondence between the piecewise and cubic stiffnesses within the designed range. Even outside the designed range, the frequency of the piecewise stiffness continues to increase, but at a lower rate than the cubic. This means that the piecewise stiffness will still perform similarly to the cubic for some higher amplitudes within a boundary of about 20 %.

Appendix F. Harmonics study

To investigate whether the single-frequency assumption of the CxA holds, the Matlab harmonic balancing (HB) numerical toolbox called MANLAB [96] is used to investigate the presence of higher harmonics of the forcing frequency. In the HB method, 50 harmonics are investigated. Figure F.22 shows the result, with RMS computed for 50 harmonics for HB. It shows that CxA approximates the result, with the biggest difference for a high force, where the IRC is attached. As the attachment of the IRC is not desired, it is safe to claim that a single-harmonic assumption is suitable within the desired operation.

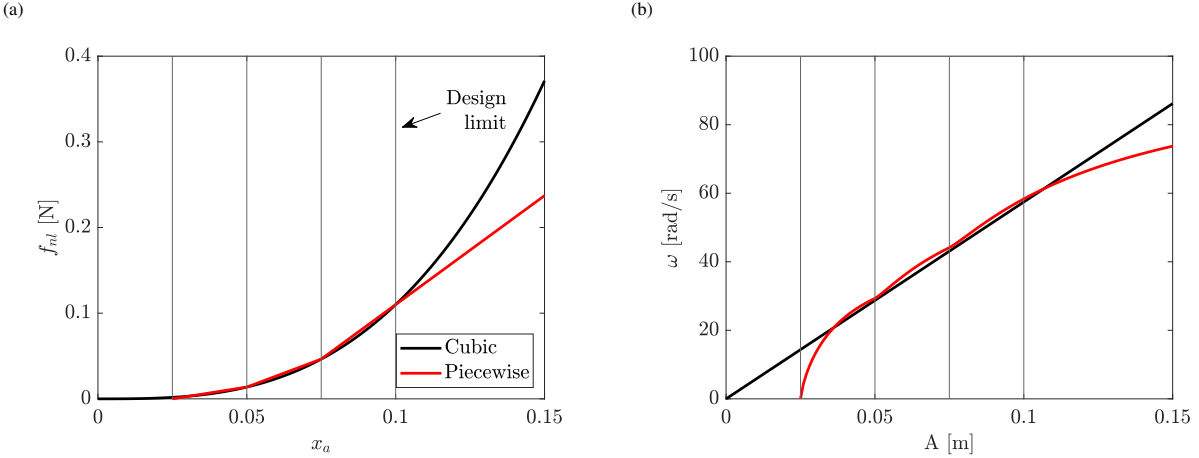


Figure E.21: (a) The comparison of the nonlinear stiffness characteristics in this paper and (b) the corresponding frequency-amplitude relation.

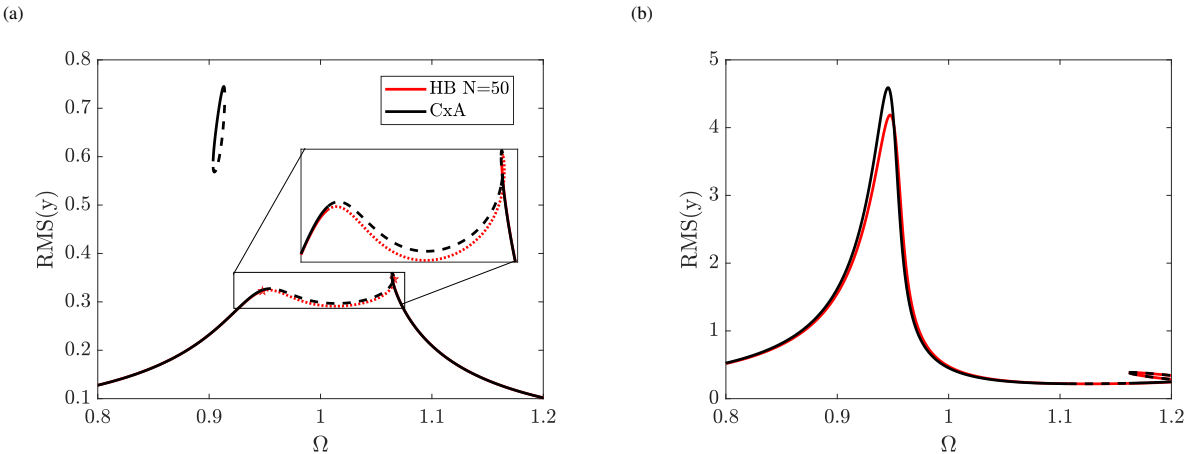


Figure F.22: Comparing the CxA and HB method (using MANLAB) with 50 harmonics, (a) for $\bar{P} = 0.73$ and (b) for $\bar{P} = 2$.

References

- [1] C. S. Keeney, S. Shih, Prediction and control of heavy duty powertrain torsional vibration, *SAE transactions* (1992). doi:10.4271/922481.
- [2] L. S. Dorfman, M. Trubelja, Torsional monitoring of turbine-generators for incipient failure detection, in: *Proceedings of the 6th EPRI Steam Turbine/Generator Workshop*, Citeseer, 1999, pp. 1–6.
- [3] M. A. Corbo, C. P. Cook, Torsional vibration analysis of synchronous motor-driven turbomachinery, in: *Proceedings of the 29th Turbomachinery Symposium*, 2000, pp. 161–176. doi:10.21423/R1H37M.
- [4] L. Beneduce, G. Caruso, D. Iannuzzi, F. Maceri, E. Pagano, L. Piegari, Analysis of a structural failure mode arising in cage rotors of induction machines, *Electrical Engineering* 93 (2011) 179–191. doi:10.1007/s00202-011-0204-8.
- [5] S. Luo, S. Wu, Fatigue failure analysis of rotor compressor blades concerning the effect of rotating stall and surge, *Engineering Failure Analysis* 68 (2016) 1–9. doi:10.1016/j.engfailanal.2016.05.021.
- [6] H. Frahm, Device for damping vibrations of bodies, 989958, United States (1911).
- [7] J. P. Den Hartog, *Mechanical vibrations*, Courier Corporation, 1985.
- [8] N. Olgac, B. Holm-Hansen, Tunable Active Vibration Absorber: The Delayed Resonator, *Journal of Dynamic Systems, Measurement, and Control* 117 (4) (1995) 513–519. doi:10.1115/1.2801108.
- [9] S. M. R. Rasid, T. Mizuno, Y. Ishino, M. Takasaki, M. Hara, D. Yamaguchi, Design and control of active vibration isolation system with an

- active dynamic vibration absorber operating as accelerometer, Journal of Sound and Vibration 438 (2019) 175–190. doi:10.1016/j.jsv.2018.09.037.
- [10] X. Wang, B. Yang, Transient vibration control using nonlinear convergence active vibration absorber for impulse excitation, Mechanical Systems and Signal Processing 117 (2019) 425–436. doi:10.1016/j.ymssp.2018.07.038.
- [11] K. Kraus, Z. Šíka, P. Beneš, J. Krivošej, T. Vyhlídal, Mechatronic robot arm with active vibration absorbers, Journal of Vibration and Control 26 (13-14) (2020) 1145–1156. doi:10.1177/1077546320918488.
- [12] J.-H. Koo, M. Ahmadian, M. Setareh, T. Murray, In Search of Suitable Control Methods for Semi-Active Tuned Vibration Absorbers, Journal of Vibration and Control 10 (2) (2004) 163–174. doi:10.1177/1077546304032020.
- [13] X. Liu, X. Feng, Y. Shi, Y. Wang, Z. Shuai, Development of a Semi-Active Electromagnetic Vibration Absorber and Its Experimental Study, Journal of Vibration and Acoustics 135 (051015) (Jun. 2013). doi:10.1115/1.4023952.
- [14] F. Weber, Semi-active vibration absorber based on real-time controlled MR damper, Mechanical Systems and Signal Processing 46 (2) (2014) 272–288. doi:10.1016/j.ymssp.2014.01.017.
- [15] F. Weber, Optimal semi-active vibration absorber for harmonic excitation based on controlled semi-active damper, Smart Materials and Structures 23 (9) (2014) 095033. doi:10.1088/0964-1726/23/9/095033.
- [16] P. Gao, C. Xiang, H. Liu, P. Walker, N. Zhang, Design of the frequency tuning scheme for a semi-active vibration absorber, Mechanism and Machine Theory 140 (2019) 641–653. doi:10.1016/j.mechmachtheory.2019.06.025.
- [17] A. Schmidt, *Dual-mass flywheel*, 7082855, United States (2006).
- [18] F. T. Wu, C. C. Cheng, Design and analysis of a speed-dependent torsional vibration absorber, Proceedings of the Institution of Mechanical Engineers, Part D: Journal of Automobile Engineering 220 (6) (2006) 763–774. doi:10.1243/09544070JAUT057.
- [19] M. Zink, M. Hausner, The centrifugal pendulum-type absorber-application, ATZ worldwide 111 (2009) 42–47. doi:10.1007/BF03225088.
- [20] N. Ichikawa, T. Suzuki, T. Atsumi, *Crank damper pulley structure for the internal combustion engine of a car*, 4710152, United States (1987).
- [21] Y. Starovetsky, O. Gendelman, Strongly modulated response in forced 2dof oscillatory system with essential mass and potential asymmetry, Physica D: Nonlinear Phenomena 237 (13) (2008) 1719–1733. doi:10.1016/j.physd.2008.01.019.
- [22] O. Gendelman, Y. Starovetsky, M. Feldman, Attractors of harmonically forced linear oscillator with attached nonlinear energy sink i: description of response regimes, Nonlinear Dynamics 51 (2008) 31–46. doi:10.1007/s11071-006-9167-0.
- [23] Dekemele, Kevin, Performance measures for nonlinear energy sinks in mitigating single and multi-mode vibrations : theory, simulation and implementation, Ph.D. thesis, Ghent University (2021).
- [24] A. F. Vakakis, O. V. Gendelman, L. A. Bergman, D. M. McFarland, G. Kerschen, Y. S. Lee, Nonlinear targeted energy transfer in mechanical and structural systems, Vol. 156, Springer Science & Business Media, 2008. doi:10.1007/978-1-4020-9130-8.
- [25] D. Quinn, R. Rand, J. Bridge, The Dynamics of Resonant Capture, in: A. K. Bajaj, S. W. Shaw (Eds.), *Advances in Nonlinear Dynamics: Methods and Applications*, Springer Netherlands, Dordrecht, 1995, pp. 1–20. doi:10.1007/978-94-011-0367-1_1.
- [26] G. Kerschen, Y. S. Lee, A. F. Vakakis, D. M. McFarland, L. A. Bergman, Irreversible Passive Energy Transfer in Coupled Oscillators with Essential Nonlinearity, SIAM Journal on Applied Mathematics 66 (2) (2005) 648–679. doi:10.1137/040613706.
- [27] D. Hong, T. L. Hill, S. A. Neild, Understanding targeted energy transfer from a symmetry breaking perspective, Proceedings of the Royal Society A: Mathematical, Physical and Engineering Sciences 477 (2251) (2021) 20210045. doi:10.1098/rspa.2021.0045.
- [28] O. V. Gendelman, E. Gourdon, C. H. Lamarque, Quasiperiodic energy pumping in coupled oscillators under periodic forcing, Journal of Sound and Vibration 294 (4) (2006) 651–662. doi:10.1016/j.jsv.2005.11.031.
- [29] G. Gatti, M. J. Brennan, I. Kovacic, On the interaction of the responses at the resonance frequencies of a nonlinear two degrees-of-freedom system, Physica D: Nonlinear Phenomena 239 (10) (2010) 591–599. doi:<https://doi.org/10.1016/j.physd.2010.01.006>.
- [30] R. J. Kuether, L. Renson, T. Detroux, C. Grappasonni, G. Kerschen, M. S. Allen, Nonlinear normal modes, modal interactions and isolated resonance curves, Journal of Sound and Vibration 351 (2015) 299–310. doi:10.1016/j.jsv.2015.04.035.
- [31] A. F. Vakakis, Inducing passive nonlinear energy sinks in vibrating systems, Journal of Vibration and Acoustics 123 (3) (2001) 324–332. doi:10.1115/1.1368883.
- [32] F. Nucera, F. L. Iacono, D. M. McFarland, L. Bergman, A. Vakakis, Application of broadband nonlinear targeted energy transfers for seismic mitigation of a shear frame: Experimental results, Journal of sound and vibration 313 (1-2) (2008) 57–76. doi:10.1016/j.jsv.2010.01.020.
- [33] N. E. Wierschem, J. Luo, M. Al-Shudeifat, S. Hubbard, R. Ott, L. A. Fahnestock, D. D. Quinn, D. M. McFarland, B. Spencer Jr, A. Vakakis, et al., Experimental testing and numerical simulation of a six-story structure incorporating two-degree-of-freedom nonlinear energy sink, Journal of Structural Engineering 140 (6) (2014) 04014027. doi:10.1061/(ASCE)ST.1943-541X.00009.
- [34] A. S. Saeed, M. A. AL-Shudeifat, W. J. Cantwell, A. F. Vakakis, Two-dimensional nonlinear energy sink for effective passive seismic mitigation, Communications in Nonlinear Science and Numerical Simulation 99 (2021) 105787. doi:10.1016/j.cnsns.2021.105787.
- [35] J. Fu, S. Wan, P. Zhou, J. Shen, M. Loccufier, K. Dekemele, Effect of magnetic-spring bi-stable nonlinear energy sink on vibration and

- damage reduction of concrete double-column piers: Experimental and numerical analysis, *Engineering Structures* 303 (2024) 117517. doi:10.1016/j.engstruct.2024.117517.
- [36] B. Bergeot, S. Bellizzi, B. Cochelin, Passive suppression of helicopter ground resonance using nonlinear energy sinks attached on the helicopter blades, *Journal of Sound and Vibration* 392 (2017) 41–55. doi:10.1016/j.jsv.2016.12.039.
- [37] K. Yang, Y.-W. Zhang, H. Ding, T.-Z. Yang, Y. Li, L.-Q. Chen, Nonlinear Energy Sink for Whole-Spacecraft Vibration Reduction, *Journal of Vibration and Acoustics* 139 (021011) (Feb. 2017). doi:10.1115/1.4035377.
- [38] I. P. Wall, M. R. Amoozgar, A. A. Popov, Aeroelasticity of an aircraft wing with nonlinear energy sink, *Aerospace Science and Technology* 155 (2024) 109684. doi:10.1016/j.ast.2024.109684.
- [39] A. Nankali, H. Surampalli, Y. S. Lee, T. Kalma'r-Nagy, Suppression of Machine Tool Chatter Using Nonlinear Energy Sink, in: ASME 2011 International Design Engineering Technical Conferences and Computers and Information in Engineering Conference, American Society of Mechanical Engineers Digital Collection, 2012, pp. 1215–1223. doi:10.1115/DETC2011-48502.
- [40] B. Peng, X. Yan, J. Du, Suppress the vibration of tool system in milling process, *AIP Advances* 12 (5) (2022) 055018. doi:10.1063/5.0091935.
- [41] M. Weiss, B. Vaurigaud, A. Ture Savadkoohi, C.-H. Lamarque, Vertical vibration mitigation of a bridge cable using a non smooth absorber under gravity, in: *Experimental Vibration Analysis for Civil Structures*, Springer International Publishing, Cham, 2018, pp. 505–513.
- [42] F. Georgiades, A. Vakakis, Dynamics of a linear beam with an attached local nonlinear energy sink, *Communications in Nonlinear Science and Numerical Simulation* 12 (5) (2007) 643–651. doi:10.1016/j.cnsns.2005.07.003.
- [43] K. V. Avramov, O. V. Gendelman, On interaction of vibrating beam with essentially nonlinear absorber, *Meccanica* 45 (3) (2010) 355–365. doi:10.1007/s11012-009-9252-9.
- [44] Y. Qiao, G. Yao, Subsonic aeroelastic stability analysis and vibration control of a plate by using nonlinear energy sink, *International Journal of Structural Stability and Dynamics* 24 (24) (2024) 2450273. doi:10.1142/S0219455424502730.
- [45] C. Wang, G. Yao, M. Liu, Passive vibration control of subsonic thin plate via nonlinear capacitance and negative capacitance coupled piezoelectric shunt damping, *Thin-Walled Structures* 198 (2024) 111656. doi:10.1016/j.tws.2024.111656.
- [46] G. Yao, Y. Qiao, Vibration suppression and energy absorption of plates in subsonic airflow using an energy harvester enhanced nonlinear energy sink, *Journal of Vibration and Control* 29 (9-10) (2023) 2301–2315. doi:10.1177/10775463221077779.
- [47] Z. Lu, Z. Wang, Y. Zhou, X. Lu, Nonlinear dissipative devices in structural vibration control: A review, *Journal of Sound and Vibration* 423 (2018) 18–49. doi:10.1016/j.jsv.2018.02.052.
- [48] H. Ding, L. Q. Chen, Designs, analysis, and applications of nonlinear energy sinks, *Nonlinear Dynamics* 100 (4) (2020) 3061–3107. doi:10.1007/s11071-020-05724-1.
- [49] G. Kerschen, J. J. Kowtko, D. M. McFarland, L. A. Bergman, A. F. Vakakis, Theoretical and experimental study of multimodal targeted energy transfer in a system of coupled oscillators, *Nonlinear Dynamics* 47 (2007) 285–309. doi:10.1007/s11071-006-9073-5.
- [50] D. Qiu, S. Seguy, M. Paredes, Tuned nonlinear energy sink with conical spring: design theory and sensitivity analysis, *Journal of Mechanical Design* 140 (1) (2018) 011404. doi:10.1115/1.4038304.
- [51] K. Dekemele, G. Habib, Inverted resonance capture cascade: modal interactions of a nonlinear energy sink with softening stiffness, *Nonlinear Dynamics* 111 (11) (2023) 9839–9861. doi:10.1007/s11071-023-08423-9.
- [52] S. Zhang, J. Zhou, H. Ding, K. Wang, D. Xu, Fractional nonlinear energy sinks, *Applied Mathematics and Mechanics* 44 (5) (2023) 711–726. doi:10.1007/s10483-023-2984-9.
- [53] S. Zhang, J. Zhou, H. Ding, K. Wang, Micro-vibration mitigation of a cantilever beam by one-third power nonlinear energy sinks, *Aerospace Science and Technology* 153 (2024) 109409. doi:10.1016/j.ast.2024.109409.
- [54] H. Venugopal, K. Dekemele, M. Loccufier, Vibration reduction in an unbalanced rotor system using nonlinear energy sinks with varying stiffness, in: *Proceedings of the 11th IFToMM International Conference on Rotordynamics*, Springer International Publishing, Cham, 2024, pp. 358–373. doi:10.1007/978-3-031-40455-9_30.
- [55] K. Dekemele, G. Habib, M. Loccufier, The periodically extended stiffness nonlinear energy sink, *Mechanical Systems and Signal Processing* 169 (2022) 108706. doi:10.1016/j.ymssp.2021.108706.
- [56] K. Dekemele, G. Habib, M. Loccufier, Vibration mitigation with a nonlinear energy sink having periodically extended stiffness, in: *ISMA2022 Conference on Noise and Vibration Engineering*, 2022, pp. 4044–405.
- [57] G. Habib, F. Romeo, The tuned bistable nonlinear energy sink, *Nonlinear Dynamics* 89 (1) (2017) 179–196. doi:10.1007/s11071-017-3444-y.
- [58] K. Dekemele, Tailored nonlinear stiffness and geometric damping: Applied to a bistable vibration absorber, *International Journal of Non-Linear Mechanics* 157 (2023) 104548. doi:10.1016/j.ijnonlinmec.2023.104548.
- [59] S. Fang, K. Chen, J. Xing, S. Zhou, W.-H. Liao, Tuned bistable nonlinear energy sink for simultaneously improved vibration suppression and energy harvesting, *International Journal of Mechanical Sciences* 212 (2021) 106838. doi:10.1016/j.ijmecsci.2021.106838.

- [60] L. Chen, X. Liao, G. Xia, B. Sun, Y. Zhou, Variable-potential bistable nonlinear energy sink for enhanced vibration suppression and energy harvesting, International Journal of Mechanical Sciences 242 (2023) 107997. doi:10.1016/j.ijmecsci.2022.107997.
- [61] X. Liao, L. Chen, H. Lee, A customizable cam-typed bistable nonlinear energy sink, International Journal of Mechanical Sciences 271 (2024) 109305. doi:10.1016/j.ijmecsci.2024.109305.
- [62] Y. cheng Zeng, H. Ding, J.-C. Ji, X.-J. Jing, L.-Q. Chen, A tristable nonlinear energy sink to suppress strong excitation vibration, Mechanical Systems and Signal Processing 202 (2023) 110694. doi:10.1016/j.ymssp.2023.110694.
- [63] Y.-c. Zeng, H. Ding, A tristable nonlinear energy sink, International Journal of Mechanical Sciences 238 (2023) 107839. doi:10.1016/j.ijmecsci.2022.107839.
- [64] H. Chen, Y. Zeng, H. Ding, S. Lai, L. Chen, Dynamics and vibration reduction performance of asymmetric tristable nonlinear energy sink, Applied Mathematics and Mechanics 45 (3) (2024) 389–406. doi:10.1007/s10483-024-3095-9.
- [65] J. Wang, G. Yao, Multi-directional vibration isolation performances of a scissor-like structure with nonlinear hybrid spring stiffness, Nonlinear Dynamics 112 (11) (2024) 8871–8888. doi:10.1007/s11071-024-09561-4.
- [66] J. Wang, G. Yao, A3-DOF frog-inspired quasi-zero stiffness isolator and its vibration control performance, Aerospace Science and Technology 149 (2024) 109163. doi:10.1016/j.ast.2024.109163.
- [67] O. V. Gendelman, Bifurcations of nonlinear normal modes of linear oscillator with strongly nonlinear damped attachment, Nonlinear Dynamics 37 (2004) 115–128. doi:10.1023/B:NODY.0000042911.49430.25.
- [68] Y. Starovetsky, O. Gendelman, Vibration absorption in systems with a nonlinear energy sink: Nonlinear damping, Journal of Sound and Vibration 324 (3) (2009) 916–939. doi:10.1016/j.jsv.2009.02.052.
- [69] M. Krack, J. Gross, Harmonic balance for nonlinear vibration problems, Vol. 1, Springer, 2019. doi:10.1007/978-3-030-14023-6.
- [70] L. I. Manevitch, Complex Representation of Dynamics of Coupled Nonlinear Oscillators, Springer US, Boston, MA, 1999. doi:10.1007/978-1-4615-4799-0_24.
- [71] V. V. Smirnov, L. I. Manevitch, Complex envelope variable approximation in nonlinear dynamics, Russian Journal Of Nonlinear Dynamics 16 (2020) 491–515. doi:10.48550/arXiv.2004.08354.
- [72] A. Haris, E. Motato, S. Theodossiades, H. Rahnejat, P. Kelly, A. Vakakis, L. A. Bergman, D. M. McFarland, A study on torsional vibration attenuation in automotive drivetrains using absorbers with smooth and non-smooth nonlinearities, Applied Mathematical Modelling 46 (2017) 674–690. doi:10.1016/j.apm.2016.09.030.
- [73] A. Haris, P. Alevras, M. Mohammadpour, S. Theodossiades, M. O’Mahony, Design and validation of a nonlinear vibration absorber to attenuate torsional oscillations of propulsion systems, Nonlinear Dynamics 100 (2020) 33–49. doi:10.1007/s11071-020-05502-z.
- [74] Y. Cao, Z. Li, J. Dou, R. Jia, H. Yao, An inerter nonlinear energy sink for torsional vibration suppression of the rotor system, Journal of Sound and Vibration 537 (2022) 117184. doi:10.1016/j.jsv.2022.117184.
- [75] Y. Cao, H. Yao, H. Li, J. Dou, Torsional vibration dynamics of a gear-shafting system attaching a nonlinear energy sink, Mechanical Systems and Signal Processing 176 (2022) 109172. doi:10.1016/j.ymssp.2022.109172.
- [76] Y. Cao, H. Yao, J. Dou, S. Han, Optimal design for torsional vibration suppression of non-smooth NES, Journal of Mechanical Science and Technology 36 (11) (2022) 5399–5412. doi:10.1007/s12206-022-1006-9.
- [77] Y. Cao, H. Yao, J. Dou, R. Bai, A multi-stable nonlinear energy sink for torsional vibration of the rotor system, Nonlinear Dynamics 110 (2) (2022) 1253–1278. doi:10.1007/s11071-022-07681-3.
- [78] J. Dou, H. Yao, Y. Cao, Z. Wang, Permanent magnet based nonlinear energy sink for torsional vibration suppression of rotor systems, International Journal of Non-Linear Mechanics 149 (2023) 104321. doi:10.1016/j.ijnonlinmec.2022.104321.
- [79] J. Dou, Z. Li, Y. Cao, H. Yao, R. Bai, Magnet based bi-stable nonlinear energy sink for torsional vibration suppression of rotor system, Mechanical Systems and Signal Processing 186 (2023) 109859. doi:10.1016/j.ymssp.2022.109859.
- [80] J. Dou, H. Yao, Y. Cao, S. Han, R. Bai, Enhancement of bistable nonlinear energy sink based on particle damper, Journal of Sound and Vibration 547 (2023) 117547. doi:10.1016/j.jsv.2022.117547.
- [81] Y. Cao, G. Yan, J. Lu, W. Zhang, Suppression of multi-modal torsional vibration of the long-shafting rotor system with nonlinear piecewise NES, International Journal of Non-Linear Mechanics 159 (2024) 104617. doi:10.1016/j.ijnonlinmec.2023.104617.
- [82] Y. Cao, G. Yan, H. Yao, J. Lu, W. Zhang, Resonance capture cascading of non-smooth nes to mitigate multi-modal torsional vibration of MDOF rotor system, Nonlinear Dynamics 113 (9) (2025) 9305–9330. doi:10.1007/s11071-024-10631-w.
- [83] K. Ma, J. Du, H. Zhang, Y. Liu, X. Chen, A comparative study on the torsional vibration suppression of rotor system using variable steady state nonlinear energy sink, Chaos, Solitons & Fractals 185 (2024) 115144. doi:10.1016/j.chaos.2024.115144.
- [84] Y. A. Kuznetsov, R. J. Sacker, Neimark-Sacker bifurcation, Scholarpedia 3 (5) (2008) 1845, revision #91556. doi:10.4249/scholarpedia.1845.
- [85] K. Dekemele, C. Giraud-Audine, O. Thomas, A piezoelectric nonlinear energy sink shunt for vibration damping, Mechanical Systems and Signal Processing 220 (2024) 111615. doi:10.1016/j.ymssp.2024.111615.

- [86] K. Dekemele, G. Habib, Softening versus hardening nonlinear energy sinks: forced vibration control and isolated resonance curves, *Nonlinear Dynamics* (2025) 1–20doi:10.1007/s11071-025-11164-6.
- [87] F. Orban, Damping of materials and members in structures, in: *Journal of Physics: Conference Series*, Vol. 268, IOP Publishing, 2011, p. 012022.
- [88] V. Terent'ev, Endurance limit of metals and alloys, *Metal Science and Heat Treatment* 50 (1) (2008) 88–96.
- [89] R. Budynas, K. Nisbett, *Shigley's Mechanical Engineering Design*, McGraw-Hill Education, 2010.
- [90] A. Koutsis, Development of a damping identification tool for machine design, Master's thesis, Ghent University (2018).
URL <https://lib.ugent.be/catalog/rug01:002494493>
- [91] K. Dekemele, P. Van Torre, M. Loccufier, Design, construction and experimental performance of a nonlinear energy sink in mitigating multi-modal vibrations, *Journal of Sound and Vibration* 473 (2020) 115243. doi:10.1016/j.jsv.2020.115243.
- [92] J. Fu, S. Wan, W. Li, J. Shen, H. Venugopal, M. Loccufier, K. Dekemele, Vibration control of a cantilever beam coupled with magnetic tri-stable nonlinear energy sink, *Nonlinear Dynamics* 112 (17) (2024) 14829–14851. doi:<https://doi.org/10.1007/s11071-024-09849-5>.
- [93] L. Mesny, S. Baguet, S. Chesné, Nonlinear vibration of a sliding-mode-controlled structure: Simulation and experiment, *Mechanical Systems and Signal Processing* 211 (2024) 111209. doi:<https://doi.org/10.1016/j.ymssp.2024.111209>.
- [94] B. Bergeot, Effect of stochastic forcing on the dynamic behavior of a self-sustained oscillator coupled to a non-linear energy sink, *International Journal of Non-Linear Mechanics* 150 (2023) 104351. doi:10.1016/j.ijnonlinmec.2023.104351.
- [95] N. Berglund, B. Gentz, *Noise-induced phenomena in slow-fast dynamical systems: a sample-paths approach*, Springer, 2006. doi:10.1007/1-84628-186-5.
- [96] M. Debeurre, O. Thomas, MANLAB: A numerically-efficient continuation software for the periodic solution of nonlinear systems (2021).